ACS OMEGA

http://pubs.acs.org/journal/acsodf
Article

Dual Applications of Cobalt-Oxide-Grafted Carbon Quantum Dot Nanocomposite for Two Electrode Asymmetric Supercapacitors and Photocatalytic Behavior

Esakkimuthu Shanmugasundaram, Kannan Vellaisamy, Vigneshkumar Ganesan, Vimalasruthi Narayanan, Na'il Saleh,* and Stalin Thambusamy*

Cite This: *ACS Omega* 2024, 9, 14101−14117

ABSTRACT: Carbon materials, such as graphene, carbon nanotubes, and quantum-dot-doped metal oxides, are highly attractive for energy storage and environmental applications. This is due to their large surface area and efficient optical and electrochemical activity. In this particular study, a composite material of cobalt oxide and carbon quantum dots (Co_3O_4−CQD) was prepared using cobalt nitrate and ascorbic acid (carbon source) through a simple one-pot hydrothermal method. The properties of the composite material, including the functional groups, composition, surface area, and surface morphology, were evaluated by using various methods such as ultraviolet, Fourier transform infrared, X-ray diffraction, Raman, X-ray photoelectron spectroscopy, Brunauer−Emmett−Teller, scanning electron microscopy, and transmission electron microscopy analysis. The electrochemical performance of the Co_3O_4−CQD composite has been studied using a three-electrode system. The results show that at 1 A g^{-1}, the composite delivers a higher capacitance of 1209 F g^{-1}. The asymmetric supercapacitor (Co_3O_4−CQD//AC) provided 13.88 W h kg^{-1} energy and 684.65 W kg^{-1} power density with a 96% capacitance retention. The Co_3O_4−CQD composite also demonstrated excellent photocatalytic activity (90% in 60 min) for the degradation of methylene blue dye under UV irradiation, which is higher than that of pristine Co_3O_4 and CQD. This demonstrates that the Co_3O_4−CQD composite is a promising material for commercial energy storage and environmental applications.

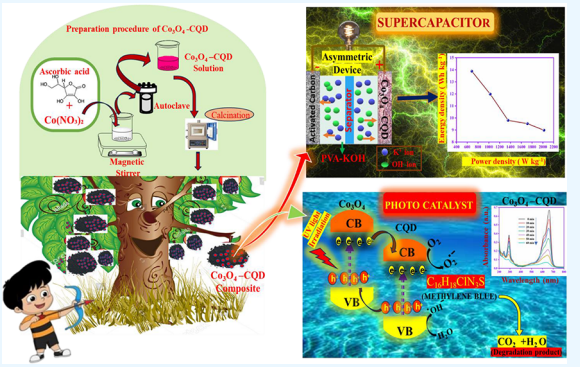

1. INTRODUCTION

The energy crisis and environmental pollution are major issues in the modern world, as they affect the quality of human life.[1] Most industries rely on nonrenewable energy sources such as coal, oil, and natural gas, which release large amounts of carbon dioxide (CO_2) gas into the environment when burned. This contributes to the environmental pollution and global warming. Therefore, it is vital to find an alternative energy source to maintain a clean and green environment. Additionally, industries, such as leather, pharmaceuticals, textiles, and plastics, release harmful organic pollutants that affect the environment. To address these challenges, scientists are focusing on developing efficient technology that can produce bifunctional materials for resolving energy and environmental issues.[2,3]

There are several techniques available for energy conversion and storage, such as solar cells,[4,5] batteries,[6,7] and supercapacitors.[8] These methods have been developed to address energy shortage problems while minimizing the environmental impact. Among them, supercapacitors (SCs)[9] have attracted the attention of the scientific community due to their unique properties, such as higher power density than batteries, long cycle stability, and rapid charge−discharge process. However, the low energy density remains a significant challenge for large-scale applications of SCs. It is well-known that commercial carbon-based materials (electric double-layer capacitors; EDLC) have a limited energy density of 10 W h kg^{-1}.[10] Pseudocapacitive materials such as transition metals,[11,12] metal−organic frameworks (MOFs),[13−15] polymers,[16] sulfides,[17] and nitrides[18] are recommended as an alternative source to EDLC materials because they deliver a higher energy density. Among transition metal oxides, those such as TiO_2,[19] WO_2,[20] NiO,[21] RuO_2,[22] MnO_4,[23] and Co_3O_4[24] are involved in faradic redox reactions and can provide higher energy density due to their higher voltage range capacity and ion diffusion properties. Among these metal oxides, cobalt oxide (Co_3O_4)[25]

Received: December 1, 2023
Revised: February 24, 2024
Accepted: February 28, 2024
Published: March 13, 2024

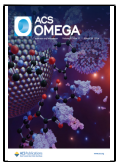

https://doi.org/10.1021/acsomega.3c09594
ACS Omega 2024, 9, 14101−14117

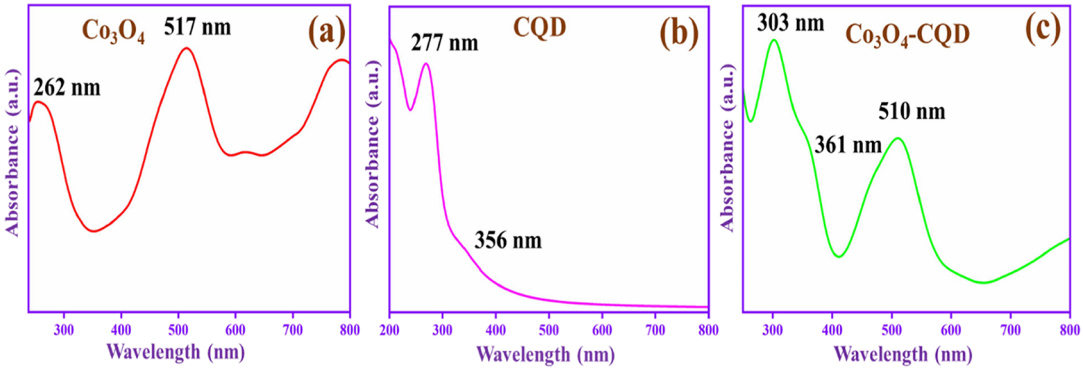

Figure 1. UV−visible spectra of (a) Co_3O_4, (b) CQD, and (c) Co_3O_4−CQD.

has been considered a promising material for supercapacitor applications due to its higher theoretical capacity (3650 F g^{-1}),[26] faradic activity, low-cost, better electrochemical performance, good cycle stability, and reversibility.

Co_3O_4 is a material that has recently gained attention in the field of photocatalytic applications due to its superior catalytic performance, high surface area, and good thermal and chemical stability. In a study by Chen et al., Co_3O_4 hollow spheres were found to be effective in degrading methyl orange dye under UV light radiation,[27] while 3D porous/urchin nanostructured Co_3O_4 prepared by pulsed laser deposition showed 81% dye degradation.[28] However, few studies have recently shown that Co_3O_4 has a high potential for photocatalytic application. Meanwhile, the Co_3O_4 has limited specific capacitance and electronic conductivity, whose properties hinder the commercial usage of these materials for SC applications.

To overcome this issue, additive materials like carbon,[29] nitrides,[30] sulfides,[31] and metals are doped with Co_3O_4. This doping process can improve the electrical and optical properties of the Co_3O_4. Particularly, carbon sources like graphene oxide (GO),[32] carbon nanotube (CNT),[33] carbon nitride (g-C_3N_4),[34] and carbon quantum dot (CQD)[35] have great potential to improve the electrochemical and optical properties of Co_3O_4 because they have an ultrafine porous structure and surface area, higher conductivity and life-cycle stability.

Among them, carbon quantum dot (CQD) is an emerging carbon material that is used in different applications such as applications including photocatalysis,[36] bioimaging,[37] sensor,[38] and photovoltaic applications[39] due to their high solubility and chemical stability. The unique properties of CQD make it an excellent additive material for improving the electrochemical and optical behaviors of metal oxides. Recently, studies have shown that metals like nickel,[40] and cobalt-doped CQD materials can provide high capacitance and exceed cyclic stability. Two cobalt-based materials, CoS-CQD[41] and Co_3O_4−Ag-CQD,[42] showed a capacitance of 808 and 1052 F g^{-1} at 1 A g^{-1}, respectively. Additionally, TiO_2-doped ascorbic acid-derived CQD is utilized as a photocatalyst for dye degradation.[43] In previous research, conducting polymers such as polyaniline, polypyrrole, and polythiophene have been combined with ascorbic acid-derived CQD for their electrochemical and photophysical properties in organic solar cell applications.[44,45]

In this work, we used an ascorbic-acid-derived CQD to improve the optical and electrical properties of Co_3O_4. We achieved this by using a one-pot hydrothermal method to produce the Co_3O_4−CQD composite. The resulting composite was characterized both photophysically and electrochemically and demonstrated multifunctional capabilities. In a three-electrode electrochemical system, the Co_3O_4−CQD composite exhibited high specific capacitance and efficient cycle stability. Additionally, the asymmetric device (Co_3O_4−CQD//AC) displayed superior energy and power density, with a recorded 13.88 W h kg^{-1} and 684.65 W kg^{-1} respectively. Furthermore, the Co_3O_4−CQD composite exhibited excellent photocatalytic activity, with a 90% dye degradation rate within 60 min under UV light, outperforming the pristine Co_3O_4. Efficient electrochemical and catalytic performance suggests Co_3O_4−CQD composite's wide use as electrode material for supercapacitors and photocatalytic material for environmental remediation.

2. EXPERIMENTAL SECTION

2.1. Chemicals. Cobalt nitrate (Co $(NO_3)_2 \cdot 6H_2O$), ascorbic acid, potassium hydroxide (KOH), and poly(vinyl alcohol) (PVA) were purchased from Sigma-Aldrich Chemicals Pvt. Ltd., India, and used without purification.

2.2. Preparation of Co_3O_4−CQD. A one-pot hydrothermal synthesis method was used to prepare Co_3O_4−CQD. First, 20 mmol of cobalt nitrate and 20 mmol of ascorbic acid were dissolved in 50 mL of water. The resulting solution was then transferred to a 100 mL Teflon autoclave and heated at 180.0 °C for 18 h. Next, the suspension solution was heated at 250 °C in a muffle furnace for 5 h. Finally, black Co_3O_4−CQD powder was collected and can be used for further purposes. The same procedure was followed to prepare Co_3O_4 and CQD separately using cobalt nitrate and ascorbic acid as precursors.

3. RESULTS AND DISCUSSION

3.1. Physicochemical Characterization. In Figure 1a, the UV−vis spectra of Co_3O_4 show two absorption peaks at 262 and 517 nm. These peaks correspond to the charge transfer processes of the Co_3O_4 spinel structure, specifically the O^{2-}−Co^{2+} and O^{2-}−Co^{3+} transitions.[46] Meanwhile, Figure 1b shows the CQD's two absorption peaks at 277 and 356 nm, which are attributed to the π−π^* transition (C=C bond) and n−π^* transition (C=O bond), respectively.[44] When Co_3O_4 and CQD are combined (Figure 1c), their absorption peaks are shifted to 303 and 510 nm. The (O^{2-}−Co^{2+}) transition is red-shifted to a longer wavelength, indicating that the CQD (π−π^* transition) interacts with the cobalt charge transfer process. Moreover, the extra peak at 361 nm confirms the CQD's n−π^* transition (carbonyl group) and the fact that Co_3O_4 is linked to the CQD.[47]

https://doi.org/10.1021/acsomega.3c09594
ACS Omega 2024, 9, 14101−14117

In Figure 2, the fluorescence spectra show that the Co_3O_4 emission peak appears at around 480 nm (green emission)

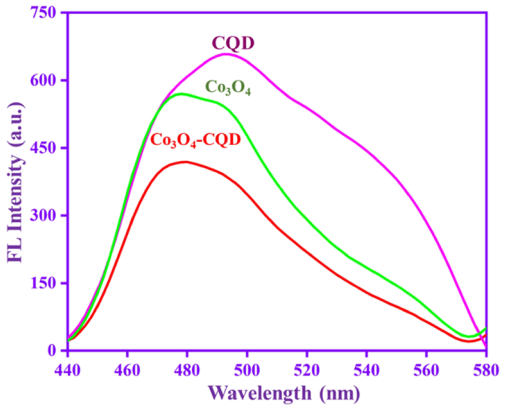

Figure 2. Fluorescence spectra of Co_3O_4, CQD, and Co_3O_4−CQD.

when excited at 365 nm. The visible region emission is due to impurities and structural defects in the nanocrystal.[48] Normally, CQD has higher fluorescence emission behavior, which is confirmed by the excitation-dependent fluorescence study (280−380 nm), as shown in Figure S1a. The fluorescence intensity of the CQD is gradually increased and the peaks are red-shifted and reaching a high intensity at 360 nm, then decreased. The intensity changes and peak shifts indicate various size carbon dots and emission trap states are presented in the CQD. In Figure S1b, the CQD is shining by various light source regions (visible and UV light) that show the yellow color in the visible region. Meanwhile, it emits strong fluorescence in the UV region (green color). The CQD has a more intense peak at 490 nm, which may be the transition of $\pi \rightarrow \pi^*$ graphitic sp^2 core in the CQD structure. The peak also appeared in Co_3O_4−CQD, but its intensity was lower than others. The low-intensity emission peak of Co_3O_4−CQD reveals that the recombination of the photogenerated electron−hole pair is highly inhibited. This poor electron−hole pair recombination can increase the photocatalytic reactions.[49]

Figure 3a shows the FT-IR spectrum of Co_3O_4, which consists of five bands ranging from 4000 to 500 cm^{-1}. The two bands at 603 and 859 cm^{-1} correspond to the characteristic bands of Co−O, which represent the rocking vibration of the metal oxide. These bands confirm the spinel structure of Co_3O_4, with Co^{3+} occupying octahedral sites and Co^{2+} occupying tetrahedral sites. The bands at 3402 and 1649 cm^{-1} represent the O−H stretching and bending vibrations of the absorbed water molecules. Additionally, the peak at 1094 cm^{-1} denotes the coordination of the Co−OH.[50,51] In Figure 3b, the O−H and C−H stretching vibration bands are presented at 3428 and 2925 cm^{-1}, respectively. The carbonyl groups C=O and C−O bands[52] are located at 1703 and 1047 cm^{-1}. The aromatic C−H stretching band appeared at 556 cm^{-1}. The Co_3O_4−CQD spectrum (Figure 3c) shows vibration bands similar to those of the Co_3O_4 spectrum but with shifted positions due to the interaction of CQD and Co_3O_4. For instance, the rocking vibration of the metal oxide is presented[53] at 584 and 862 cm^{-1}. Additionally, one band observed at 1710 cm^{-1} corresponds to the carbonyl functional group of CQD, confirming the presence of CQD in the Co_3O_4 composite.

The XRD analysis was used to characterize the phase form of Co_3O_4, CQD, and the Co_3O_4−CQD. The patterns shown in Figure 4a indicate that Co_3O_4 has a cubic structure nature, with diffraction peaks at 31.59°, 36.90°, 44.70°, 60.00°, and 65.54° corresponding to the 220, 311, 400, 511, and 440 planes of Co_3O_4 (JCPDS card no: 073-1701).[54] CQD, on the other hand, exhibits a broad diffraction peak at 24.20° (002), indicating the lattice carbon disordered structure of CQD.[55] Interestingly, the Co_3O_4 planes 220, 311, 400, 511, and 440 are also present in the Co_3O_4−CQD composite, but the position is slightly shifted and the peaks have sharply appeared. These results confirm that CQD is present in the Co_3O_4−CQD composite, where it acts as a surfactant and improves the crystalline nature of the cobalt.[47]

The composite has been confirmed by Raman spectral data. In Co_3O_4, the peak appears at 585 cm^{-1}, and the E_g and A_{1g} mode[56] of cobalt oxide is ascribed to 678 cm^{-1}, as shown in Figure 4b. The CQD has two major peaks at 1360 and 1590 cm^{-1}, which are attributed to the D and G bands. The D band corresponds to the vibration peak of the terminal graphite carbon (sp^3) planes, and the G band denotes the vibration of the hexagonal lattice of two-dimensional carbon. Moreover, the peak at 3000 cm^{-1} corresponds to the 2D band that confirms the number of sp^2 layers presented in the CQD.[57] The same type of peaks appeared in the Co_3O_4−CQD composite, which proves the carbon network presented in the Co_3O_4−CQD composite. Additionally, another three peaks at 597, 678, and 1013 cm^{-1} for the Co_3O_4−CQD are attributed to the E_g, A_{1g} symmetric stretching and the O−H [Co $(OH)_2$] deformation

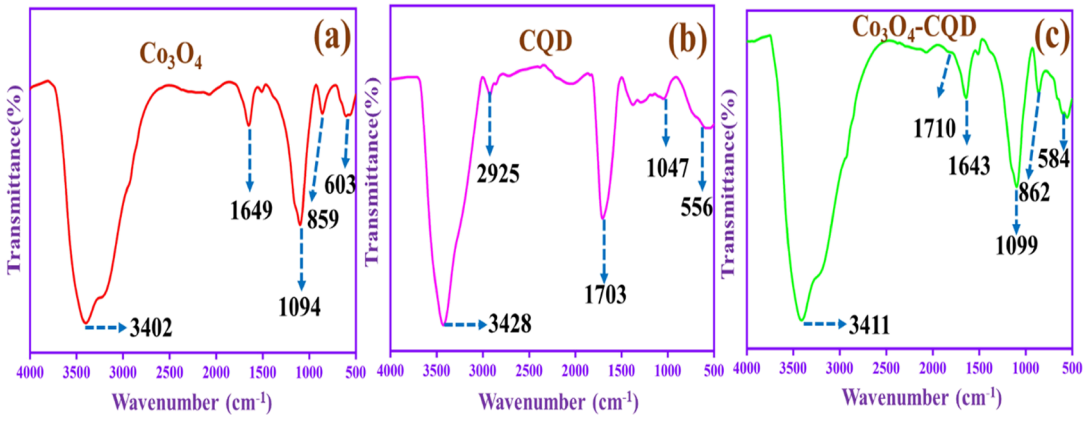

Figure 3. FT-IR spectra of (a) Co_3O_4, (b) CQD, and (c) Co_3O_4−CQD.

https://doi.org/10.1021/acsomega.3c09594
ACS Omega 2024, 9, 14101−14117

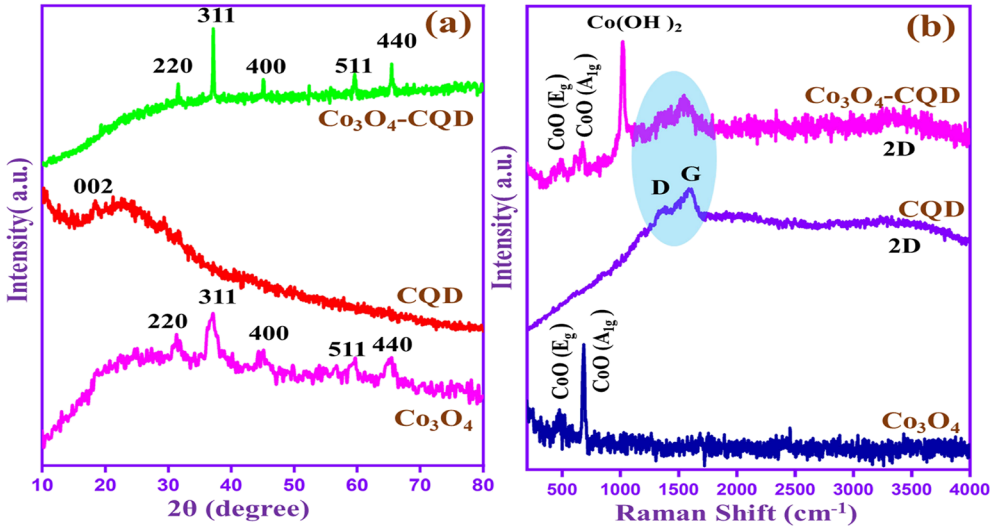

Figure 4. XRD (a) and Raman spectra (b) of Co_3O_4, CQD, and Co_3O_4−CQD.

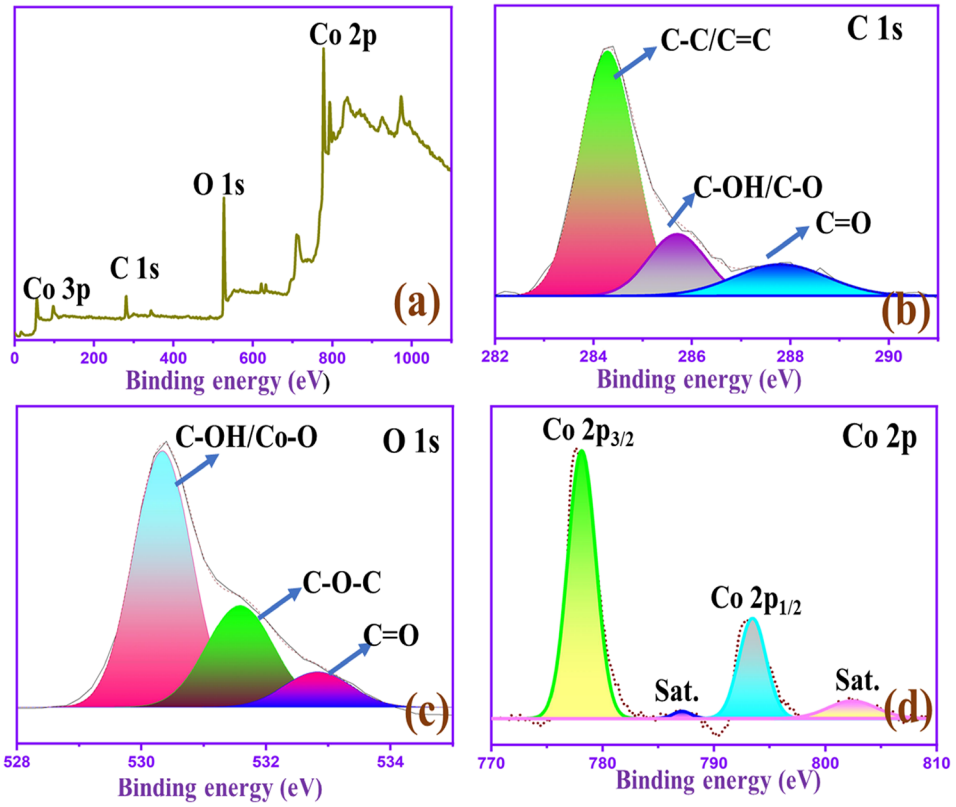

Figure 5. XPS deconvoluted spectra of Co_3O_4−CQD. (a) Survey scan, (b) C 1s, (c) O 1s, and (d) Co 2p.

mode.[58] The XRD and Raman results confirm the formation of the Co_3O_4−CQD.

X-ray photoelectron spectroscopy (XPS) analysis was used to determine the element composition and surface valence state of Co_3O_4−CQD. The composition included Co, C, H, and O elements, which were identified in the survey spectrum (Figure 5a). The peaks observed in Figure 5b at 284.23, 285.66, and 287.86 eV were attributed to different carbon bonds, such as C−C/C=C for the CQD carbon skeleton, and C−OH/C−O and C=O bonds for the surface functional groups of CQD. The O 1s spectrum in Figure 5c displayed peaks at 530.31, 531.56, and 532.82 eV, which corresponded to the C−OH/Co−O, C−O−C, and C=O bonds, respectively,[59] confirming the presence of CQD in the composite materials. Additionally, the Co 2p peaks at 778.19 and 793.63 eV in Figure 5d were attributed to the presence of Co^{2+} in $2p_{3/2}$ and $2p_{1/2}$ chemical states, respectively, which indicates the formation of cobalt oxide in the composite. The peaks at 787.12 and 802.56 denoted the satellite peak of the $2p_{3/2}$ and $2p_{1/2}$, confirming the formation of Co^{3+} on the surface.[60] Compared to Co_3O_4,[61] the Co_3O_4−CQD Co 2p region is shifted to the lower binding energies, indicating the reduction of the Co valence state due to the formation of Co−O and Co−C formation after the addition of CQD's oxygen and

https://doi.org/10.1021/acsomega.3c09594
ACS Omega 2024, 9, 14101−14117

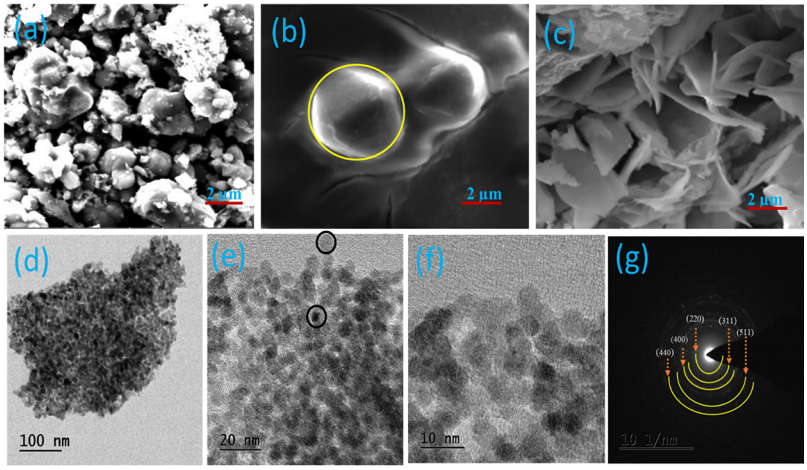

Figure 6. SEM images of (a) Co_3O_4, (b) CQD, (c) Co_3O_4−CQD, and TEM images of Co_3O_4−CQD (d−f), and SAED patterns of Co_3O_4−CQD (g).

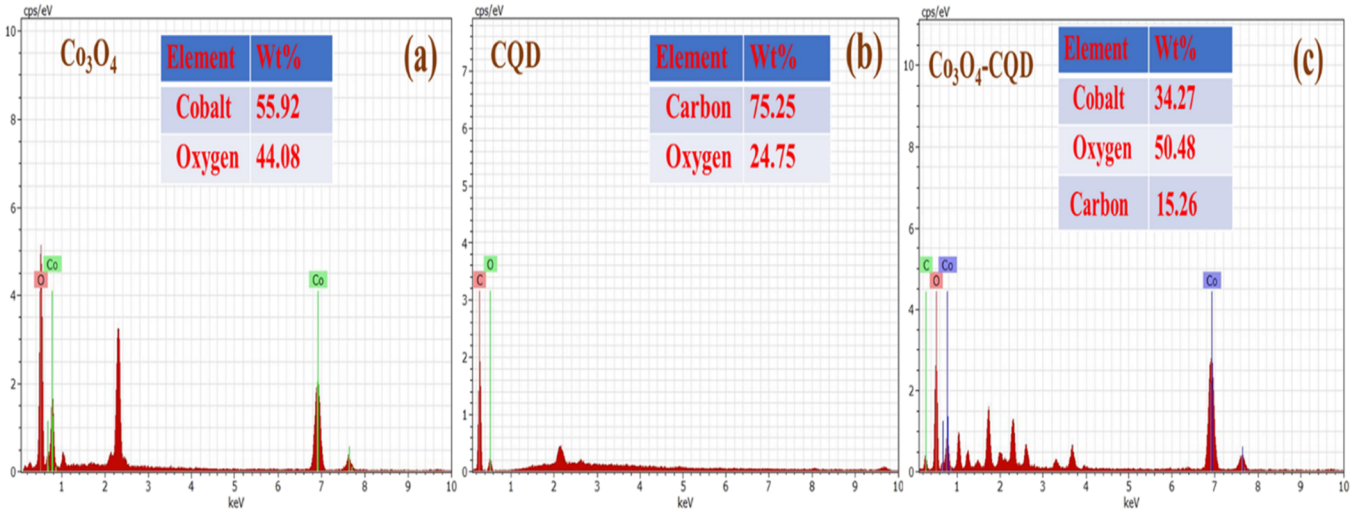

Figure 7. EDX images of (a) Co_3O_4, (b) CQD, and (c) Co_3O_4−CQD.

carbon in the Co_3O_4 skeleton structure. The CQD zeta potential value is −14 mV (Figure S2), the value confirms the CQD has a greater number of electronegative atoms so that it can easily interact with the Co atom by their surrounding electrons.[62] The formation of interstitial compound (Co−O) induces more active sites and defects, which can improve the interaction between electrode−electrolyte ions. The interaction can boost the charge transfer mobility and storage capacity of the composite material. The XPS finding illustrates the coexistence of cobalt and CQD in the Co_3O_4−CQD composite.

The structure and surface morphology of Co_3O_4, CQD, and Co_3O_4−CQD were characterized by SEM and TEM, as shown in Figure 6. Figure 6a−c displays the SEM images of Co_3O_4, CQD, and Co_3O_4−CQD, respectively. The Co_3O_4 images indicate a uniform distribution of Co_3O_4, which has a woven sphere shape, whereas the CQD has a spherical ball-shaped structure.[63] The Co_3O_4−CQD has a brush-like structure[64] which is entirely different from Co_3O_4, and this structural change is due to CQD acting as a surfactant. In addition, the side position brushes bind to each other, creating bundles.[65] The TEM images in Figure 6d−g show that the composite material has a highly porous honeycomb-like structure. The TEM image of CQD (Figure S3) shows that the CQD has a spherical shape with a diameter of 2−10 nm. The spherical shape dots are also presented in the Co_3O_4−CQD composite, representing the CQD anchored on the cobalt oxide surface. The SAED patterns of Co_3O_4−CQD values 220, 311, 222, 400, 422, 511, and 440 (inward to outward) direction confirm the binding of Co_3O_4 and CQD[54,66] to form a composite, which is consistent with the XRD result. The SEM and TEM results indicate that the Co_3O_4−CQD composite electrode can be easily exposed to the electrolyte, and its brush and mesoporous nature enhances the electrochemical performance.

The EDX analysis was used to determine the percentage of elements in the composite, as shown in Figure 7. In Co_3O_4 (Figure 7a), two peaks were observed, corresponding to the cobalt and oxygen present in the material. Using the peak intensities in the EDX profile, the amounts of cobalt and oxygen were found to be 55.92 and 44.08%, respectively.[67] The CQD, shown in Figure 7b, consists of 75.25% carbon and 24.75% oxygen. In Figure 7c, the Co_3O_4−CQD composite contains 34.27% cobalt, 50.48% oxygen, and 15.26% carbon. The carbon peaks confirm the presence of CQD in the Co_3O_4.[68]

https://doi.org/10.1021/acsomega.3c09594
ACS Omega 2024, 9, 14101−14117

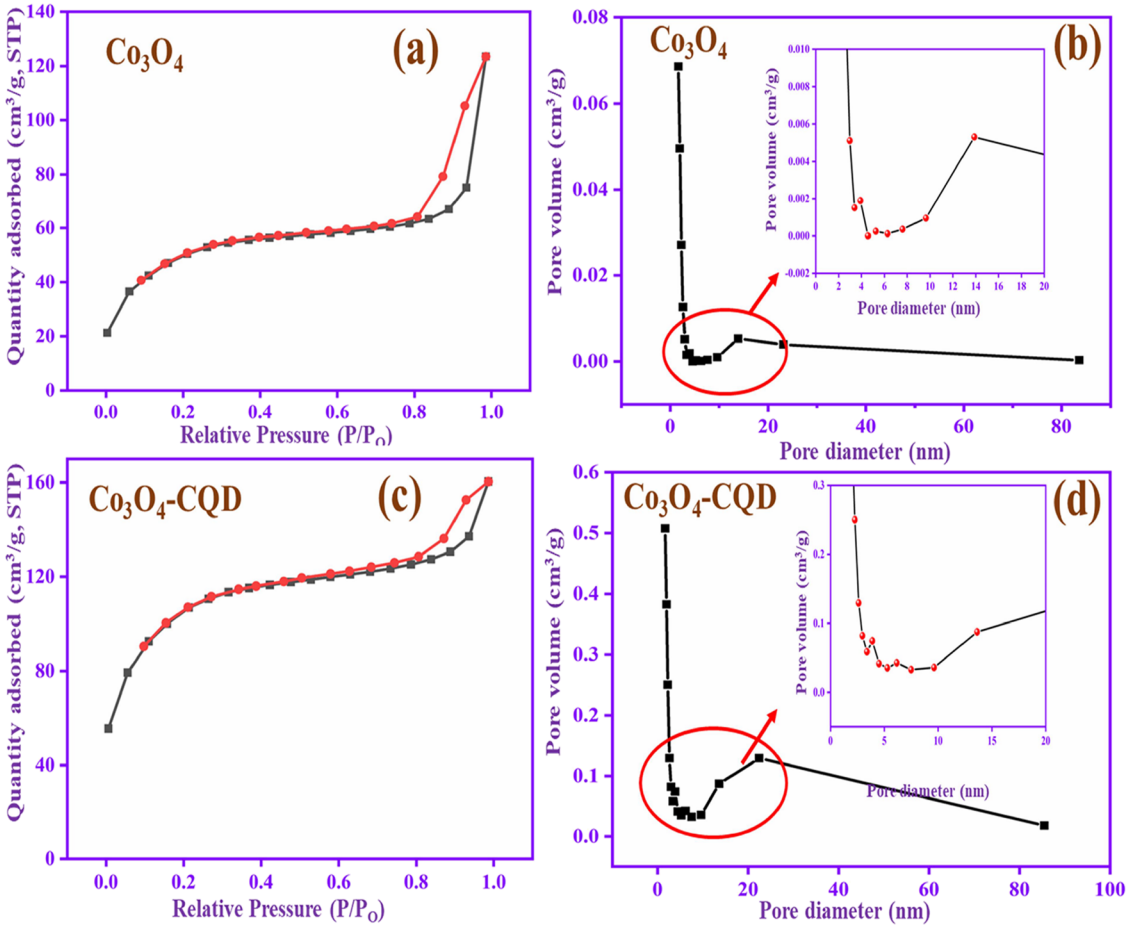

Figure 8. Nitrogen adsorption−desorption isotherms for (a) Co_3O_4 and pore size distributions of (b) Co_3O_4; nitrogen adsorption−desorption isotherms for (c) Co_3O_4−CQD, and (d) pore size distributions of Co_3O_4−CQD. The inset of (b) and (d) exhibits a magnified view of mesopore distribution.

The surface area and pore diameter of Co_3O_4 and Co_3O_4−CQD were evaluated using nitrogen adsorption and desorption isotherm measurements, specifically the Brunauer−Emmett−Teller (BET) method. Figure 8a and b show that the surface area and pore size diameter of Co_3O_4 are 127.04 m^2/g and 4.17 nm, respectively. The CQD surface area and pore size diameter (Figure S4a,b) are 9.63 m^2/g and 2.15 nm, respectively. On the other hand, the surface area of Co_3O_4−CQD (Figure 8c) is higher than that of Co_3O_4 and CQD, measuring 209.24 m^2/g, while the pore size is smaller at 2.54 nm (Figure 8d). The reason for the surface area elevation of the composite is the distribution of cobalt ions with the carbon matrix. To the best of our knowledge, the surface area of Co_3O_4−CQD is higher than previous reports based on Co_3O_4 composites.[69−71] This higher surface area is a key factor that affects the interfacial electrochemical behavior of the electrode material[72] and its photocatalytic application. Additionally, the small porous structure of Co_3O_4−CQD enhances ion diffusion in supercapacitors[73] and improves the sorption ability of dye molecules in photocatalytic applications.

3.2. Electrochemical Analysis of the Three-Electrode System. The three-electrode system's cyclic voltammogram (CV) for Ni foam, Co_3O_4, CQD, and Co_3O_4−CQD in 1 M KOH at 10 mV/s during the 0.1−0.7 V potential window is shown in Figure 9a. The Co_3O_4 current density and curve area increased while the redox peaks shifted to Ni foam and CQD. The reversible redox process in the different valent states of cobalt in the Co_3O_4 can attributed to the redox peaks. Based on earlier reports,[74,75] the electrochemical reaction mechanism involving Co_3O_4 and electrolyte anions (OH^-) can be expressed (eqs 1 and 2).

$$Co_3O_4 + OH^- + H_2O \Leftrightarrow 3CoOOH + e^- \quad (1)$$

$$CoOOH + e^- \Leftrightarrow CoO_2 + H_2O + e^- \quad (2)$$

Compared to Co_3O_4, Co_3O_4−CQD delivered a higher current density, suggesting the carbon source (CQD) can improve electrochemical active sites during that redox process. It is a well-known factor that the CV area curve is positively related to the capacitance performance.[76] The CV area curve of Co_3O_4−CQD is higher than that of Co_3O_4 which indicates that Co_3O_4−CQD has higher capacitance than Co_3O_4. Moreover, the result suggests that the CQD improves the electron transport and diffusion ion process within the Co_3O_4−CQD composite with the help of the synergistic effect, the reason the composite has higher energy storage capacity.[77]

To further investigate the charge transfer property of the Co_3O_4−CQD composite, the electrode involves different potential scan rate studies in the CV, and the results are in Figure 9b. With increasing scan rate, the position of the redox peak shifted toward the positive voltage direction due to the diffusion polarization effect, and the current range increased because of the improvement of the capacitance behavior of the

https://doi.org/10.1021/acsomega.3c09594
ACS Omega 2024, 9, 14101−14117

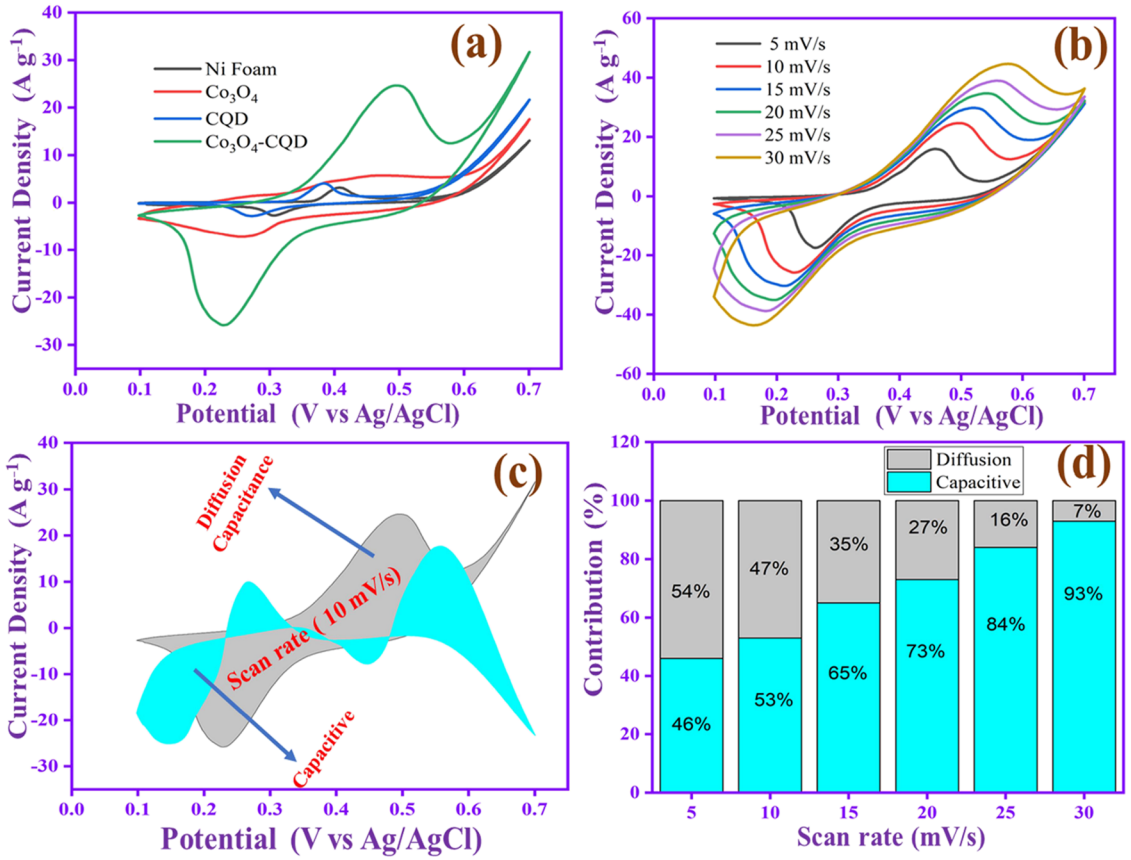

Figure 9. (a) CV study of Co_3O_4, CQD, and Co_3O_4−CQD, (b) CV different scan rate study of Co_3O_4−CQD, and (c) proportion of capacitive and diffusion capacitance for charge storage contributions of Co_3O_4−CQD at 10 mV/s. (d) Comparison of the stored charge at scan rates of 5, 10, 15, 20, 25, and 30 mV/s.

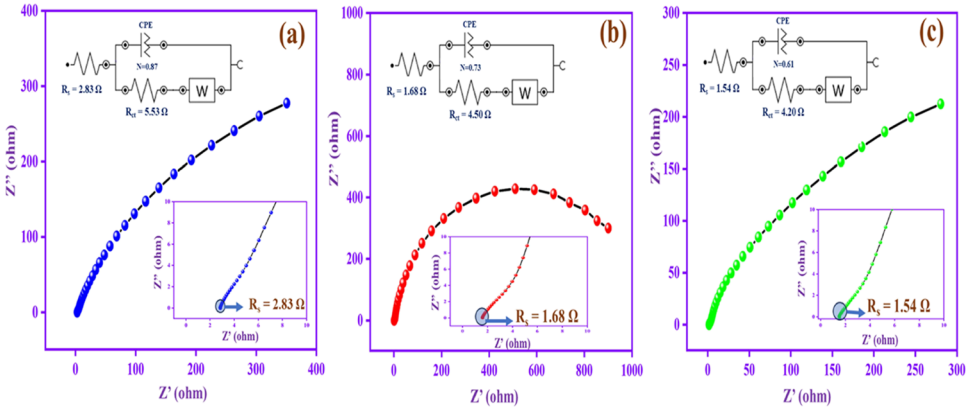

Figure 10. EIS spectra and the equivalent circuits of (a) Co_3O_4, (b) CQD, and (c) Co_3O_4−CQD.

electrode material. To identify the capacitance ratio of the Co_3O_4−CQD composite, the capacitive and diffusion behavior of the composite was investigated. The current response of the Co_3O_4−CQD composite is estimated by the separation of capacitive and diffusion-controlled processes.[78] As per the reports from the Dunn group, eq 3[79] helps to calculate the capacitive effects.

$$I_p(v) = k_1 v + k_2 v^{0.5} \quad (3)$$

where I_p denotes the current density (A g^{-1}) corresponding to the redox peaks, k_1 and k_2 denote constant coefficients, v is the scan rate (mV/s), $k_1 v$ is the current from the surface capacitance, and $k_2 v^{0.5}$ is the process of diffusion-controlled intercalation.

Figure 9c shows the capacitive (shaded region) and diffusion capacitances for charge storage contributions at 10 mV/s. It exhibits that the contribution rate of diffusion capacitance is 47% whereas the surface capacitance is 53%. Figure 9d, the contribution rates of the Co_3O_4−CQD composite in different scan rates are given in which the low scan rate (5 mV/s), the capacitive contribution, is lower (46%) than the diffusion contribution (54%). Based on the scan rate improvement, the capacitive contribution (surface capacitance) gradually increased and reached 93% at 30 mV/s. The Co_3O_4−CQD composite electrode contains higher capacitive contribution

https://doi.org/10.1021/acsomega.3c09594
ACS Omega 2024, 9, 14101−14117

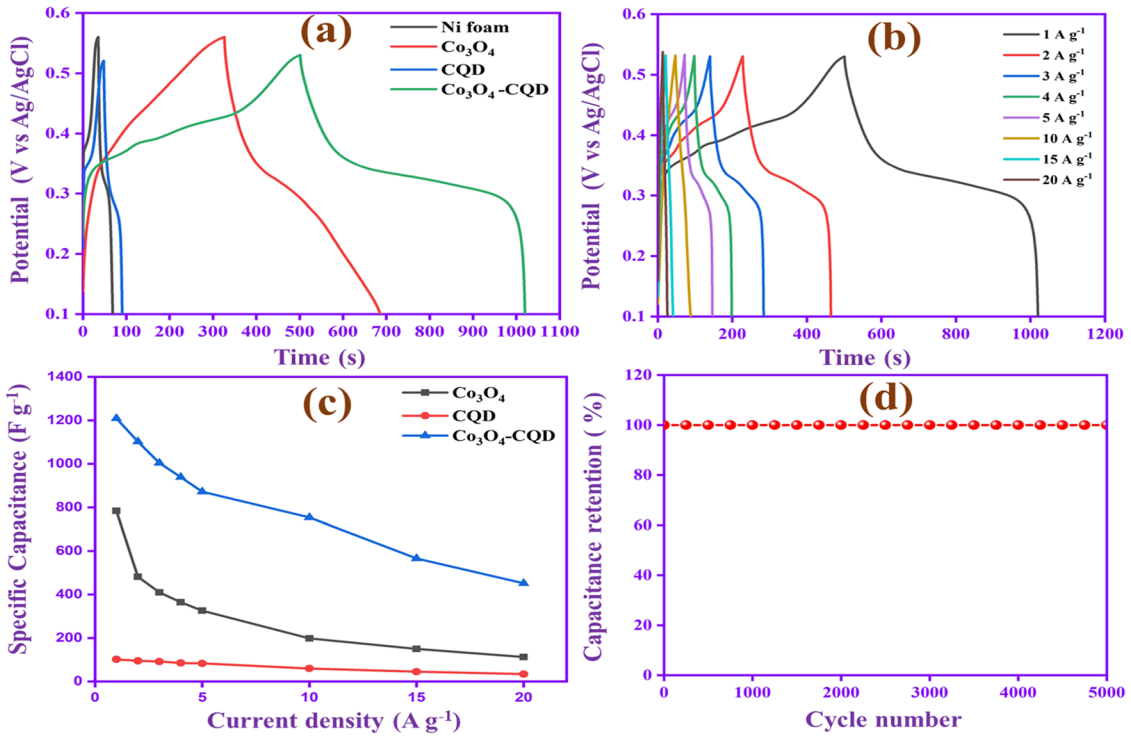

Figure 11. (a) GCD study of Co_3O_4, CQD, and Co_3O_4−CQD, (b) different current density, (c) specific capacitance values, and (d) cycle stability study of Co_3O_4−CQD.

due to the higher ion accessibility with sufficient surface-active sites[80] and rapid ions/electron migration between electrode/electrolyte interface. Based on the scan rate improvement, the capacitive contribution rate is increased which confirms the fast reaction kinetics ability[81] of the Co_3O_4−CQD electrode. It is the main factor for achieving superior rate capability and cyclic performance at high current density during charge−discharge processes.[82]

The EIS is a great tool to analyze electron transfer and kinetics of ions between the electrode and electrolyte. The Co_3O_4, CQD, and Co_3O_4−CQD impedance spectra involve an electrochemical fitting process, as exhibited in Figure 10a−c. The fitting process gives the equivalent circuits containing solution resistance (R_s), charge transfer resistance (R_{ct}), Warburg impedance element (W), and constant phase element (CPE).[83,84] A Nyquist plot has two distinct parts which include a semicircle in the higher-frequency region and a sloped straight line in the higher-frequency region.[85] The R_s values of the prepared materials are Co_3O_4 (2.83 Ω), CQD (1.68 Ω), and Co_3O_4−CQD (1.54 Ω), and the R_{ct} values are Co_3O_4 (5.53 Ω), CQD (4.50 Ω), and Co_3O_4−CQD (4.20 Ω). All among the Co_3O_4−CQD have lower R_s and R_{ct}, so the electron and charge transfer between the electrolyte and electrode is high.[86] It is a crucial factor for electrochemical energy devices since the minimum resistance can enhance the conductivity with the help of a speed redox reaction. The results are consistent with those of the CV study. Furthermore, the material porosity can generate the CPE.[87] The CPE calculated from the following (eq 4),

$$Z_{CPE} = T_{CPE}(jw)^{-n} \quad (4)$$

where n and T_{CPE} are frequency-independent constants and w is the angular frequency. The 'n' is a correction factor that is related to the electrode material roughness. The values n = 0−0.5 denote a Warburg behavior, while n = 0−1 denotes the CPE as an ideal capacitor. The Co_3O_4−CQD 'n' value is 0.61, which indicates that the electrode has ideal supercapacitor behavior (pseudo capacitance). The result reveals that the solution resistance and charge transfer between the electrode and electrolyte is more significant, the behavior is responsible for higher capacitance property.

Galvanostatic charge−discharge (GCD) analysis helps determine the capacitance behavior of the electrode materials. The Co_3O_4, CQD, and Co_3O_4−CQD specific capacitance are 784, 102, and 1209 F g^{-1} at 1 A g^{-1}. The Co_3O_4 electrode GCD curve exhibits pseudocapacitive behavior whereas the Co_3O_4−CQD curve has a hybrid capacitive nature due to the electrochemical double-layer capacitance behavior of CQD, as shown in Figure 11a. The GCD study at different current densities (1−20 A g^{-1}) is exhibited in Figure 11b. When the current density is increased (Figure 11c), the specific capacitance is gradually decreased due to the insufficient time for the Faraday reaction in the fast charge−discharge process.[88] However, Co_3O_4−CQD has 452 F g^{-1} capacitance at the 20 A g^{-1} range is 38% of the original capacitance whereas Co_3O_4 is 14% of the original capacitance, these results suggest that the CQD not only accelerates the ion and electron transport of the Co_3O_4 composite but also restrict the diffusion opposition throughout the charge−discharge processes. Long-term cyclic stability is one of the crucial parameters for commercial supercapacitor applications. As shown in Figure 11d, the Co_3O_4−CQD electrode material involves a charge−discharge cycle test at 20 A g^{-1}, and the result exhibits 100% capacitance retention after 5000 cycles. The material was also analyzed by XRD and XPS study after 5000 cycles to understand the phase and composition of the material. In the XRD spectra (Figure S5), the cobalt oxide corresponding patterns such as 220, 311, 400, 511, and 440 are presented

https://doi.org/10.1021/acsomega.3c09594
ACS Omega 2024, 9, 14101−14117

before and after cycling. The XRD spectrum has no phase change but the peaks are slightly shifted in their position which may be the addition of binding polymer and conducting carbon added in the composite. In XPS spectra of the Co_3O_4−CQD composite before cycling (Figure S6), the carbon spectrum peaks are presented at 284.03 (C−C/C=C), 286.34 (C−OH/C−O) and 288.48 eV (C=O) and the oxygen peaks located at 530.31 (C−OH/Co−O) and 531.42 eV(C−O−C), respectively. The same peaks are presented in the Co_3O_4−CQD composite after the cycling test (Figure S7). Meanwhile, the peaks of the Co spectrum (before cycle) $2p_{3/2}$ and $2p_{1/2}$ are presented at 779.90 and 795.11 eV, and the peak at 782.11 and 796.81 eV which corresponds to the Co^{2+} and Co^{3+} chemical state of cobalt oxide, respectively. After the cycle, the peaks are slightly shifted and located at (780.84 and 796.42 eV-Co^{2+}) and (785.03 and 799.56 eV-Co^{3+}) which is more similar to the before cycle. The slight intensity shift and full width at half-maximum aspects may be the substrate (Ni foam) and the addition of binding polymer in the composite. The result indicates that the material is stable, and the charge storage mechanism involved a complete reversible reaction near/on the surface of the material.

For our understanding and comparative studies for the different electrode materials, respective capacitance and its cycle stability are tabulated briefly in Table 1.

Table 1. Electrochemical Performance of Co_3O_4−CQD in Comparison with Reported Cobalt and Other Metal-Oxide-Doped CQD-Based Materials

s. no.	electrode material	capacitance	cycle stability	ref
1	CQDs/CoS_2	808 F g^{-1} at 1 A g^{-1}	98.75% (10,000)	41
2	MnO_2/CQDs/GA	721 F g^{-1} at 1 A g^{-1}	92.3% (10,000)	89
3	CuS@CD-GOH	920 F g^{-1} at 1 A g^{-1}	90%, (5000)	90
4	CuS@CQDs@C HNS	618 F g^{-1} at 1 A g^{-1}	95%, (4000)	91
5	CQD-MnO_2	189 F g^{-1} at 0.14 A g^{-1}	100%, (1200)	92
6	CQD-Bi_2O_3	343 F g^{-1} at 0.5 A g^{-1}	95%, (2500)	93
7	CQDs-MnO_2	340 F g^{-1} at 1 A g^{-1}	80%, (10,000)	94
8	RCQD/RuO_2	594 F g^{-1} at 1 A g^{-1}	96%, (5000)	95
9	NiS/C-dot	880 F g^{-1} at 2 A g^{-1}	100%, (1000)	40
10	MoS_2/NCDs	149.21 F g^{-1} at 0.5 A g^{-1}	100%, (2000)	10
11	$CuMnO_2$/GQD	520.2 F g^{-1} at 0.5 A g^{-1}	83.3% (5000)	96
12	Co_3O_4-CQD	1209 F g^{-1} at 1 A g^{-1}	100%, (5000)	this work

3.3. Electrochemical Analysis of Supercapacitor Two-Electrode System. For commercial applications, a two-electrode asymmetric supercapacitor device is fabricated by using Co_3O_4−CQD as a positive electrode and activated carbon as a negative electrode. Before solid-state analysis, the two-electrode potential window is determined by a three-electrode system using 1 M KOH as an electrolyte; it is shown in Figure 12a. The abovementioned analysis and its result suggest that the potential window of two electrodes is 0−1.6 V. Figure 12b depicts different potential window CV studies of the (Co_3O_4−CQD//AC). In Figure 12c, the CV curve current range is gradually increased and achieves a higher current range (4 mA), and it has a proper redox peak with a rectangular-shaped CV curve. The CV redox peaks are retained very well even at 100 mV/s the results suggest that the device possesses higher power capability. The EIS exhibits (Figure 12d) the semicircle that corresponds to the double layer and charges transfer resistance which is 1.69 and 9.28 Ω. The low resistance behavior confirms that the device has higher electrical conductivity due to the synergistic effect between the cobalt ion with CQD. The small R_{ct} value demonstrated the fast ion and charge transfer kinetics of the electrode−electrolyte interface.

Furthermore, the Co_3O_4−CQD//AC device potential window is analyzed and finally determined at 0.8−1.4 V, it is shown in Figure 13a. The GCD curves (0.5−10 A g^{-1}) are exhibited in Figure 13b. The capacitance value of the device is 51 F g^{-1} at 0.5 A g^{-1} and 19 F g^{-1} at 10 A g^{-1} which is calculated from the GCD curves.[60] Energy and power density are crucial merit factors in energy storage devices that help to determine the performance of SCs for real applications. In Ragone plot (Figure 13c), exhibits the relationship between the energy density and power density[97] and the values are 13.88 W h kg^{-1} energy density and 684.65 W kg^{-1} power density, respectively. The long cycling life is an essential parameter of the SCs device in which the charge−discharge measurement is repeated 5000 times at 10 A g^{-1} in the potential window 0−1.4 V as shown in Figure 13d. The capacitance range slightly decreased and delivered 96% retention after 5000 cycles; this result indicates the high electrochemical stability and the excellent performance of the device. The amorphous nature of the carbon network-induced Co_3O_4−CQD electrode material controls the volume change during the charge−discharge process that property can improve the cyclic performance of the electrode. The results suggest that this device is suitable for practical SC applications.

3.4. Photocatalytic Application. The study on the photodegradation of MB under UV irradiation is presented in Figure 14. A blank test was conducted without a catalyst, and the initial absorption spectra of MB showed a negligible decrease after 60 min of UV irradiation (Figure 14a). In the pristine Co_3O_4 test, the absorption of MB gradually decreased upon UV irradiation, as shown in Figure 14b. The absorption spectra range of MB slightly decreased after exposure to UV irradiation for 10 min in the presence of Co_3O_4. With continuous UV irradiation for 10−60 min, the MB absorption spectra considerably decreased. After 60 min of UV irradiation, the absorption intensity range decreased by approximately 50% from its initial range. This degradation pattern was observed in the pristine CQD as well, as shown in Figure 14c. However, Co_3O_4−CQD (Figure 14d) exhibited efficient degradation of MB under UV irradiation, with a 90% decrease in the absorption intensity range at 60 min. This intensity loss was higher than those observed in Co_3O_4 and CQD.

The efficiency of dye degradation rates under UV irradiation in the presence of Co_3O_4, CQD, and Co_3O_4−CQD is shown in Figure 15a,b. The photocatalytic degradation efficiency is calculated based on the initial and final absorbance range of the dye molecule.[98] The Co_3O_4−CQD composite degraded 90% of the dye in just 60 min. However, without a catalyst, pristine Co_3O_4 and CQD only degraded 3, 52, and 45%, respectively. The improved catalytic activity of the Co_3O_4−CQD composite can be attributed to its higher surface area and chemical composition. In addition, the Co_3O_4−CQD composite exhibits an enhanced photocatalytic effect due to the synergistic effect

https://doi.org/10.1021/acsomega.3c09594
ACS Omega 2024, 9, 14101−14117

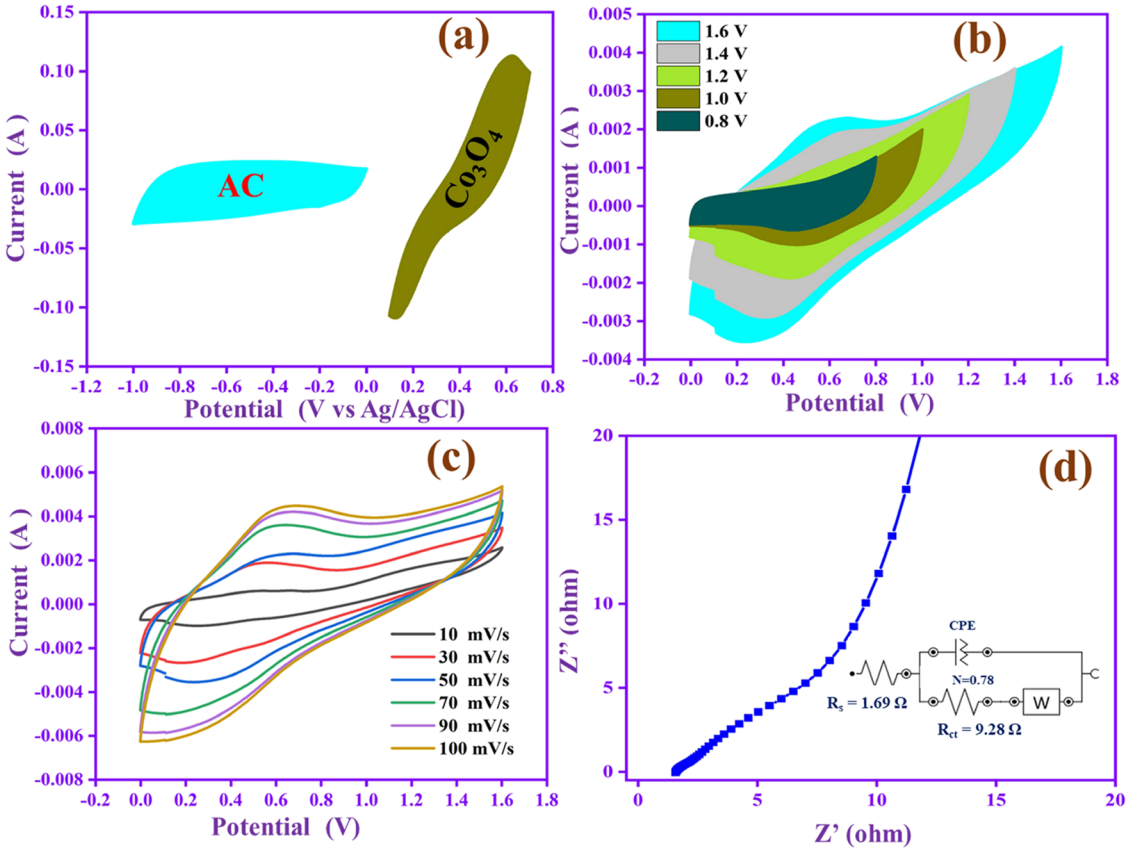

Figure 12. (a) CV study of AC and Co_3O_4−CQD at 50 mV/s in 1 M KOH in three-electrode systems, (b) different potential windows, (c) different scan rates, and (d) EIS study of Co_3O_4−CQD//AC asymmetric two electrode devices.

between CQD and Co_3O_4. This synergistic effect is explained in the electrochemical performance section, which results in improved quick charge transport and reduced recombination of electron/hole (e^-/h^+) during the photocatalytic reaction.[99] These separations of e^-/h^+ generate a greater amount of active oxygen radicals such as OH and O_2^- from H_2O and O_2, which can effectively degrade dye molecules. Moreover, the presence of CQD (carbon source) increases the surface area of the Co_3O_4−CQD composite (as demonstrated in the N_2 adsorption−desorption isotherm study), facilitating the absorption of dye molecules on the surface of the composite during degradation. The stability of the photocatalyst is a crucial aspect of its practical applications.

The study aimed to evaluate the photocatalytic reusability and stability of Co_3O_4−CQD, which underwent three consecutive cycles under UV irradiation. The results showed that the photocatalytic activity (Figure 15c) of Co_3O_4−CQD for MB dye degradation decreased by only 2% (from 90 to 88%), indicating that it is a stable photocatalyst for dye degradation. The structure stability and crystalline nature of Co_3O_4−CQD were also assessed (Figure 15d), and the XRD pattern showed no change even after three photocatalytic experiment cycles. Additionally, there was no phase transformation during UV light illumination, indicating that Co_3O_4−CQD has good chemical stability and reusability properties.

3.4.1. Plausible Mechanism for Photodegradation of Co_3O_4−CQD. The band gap analysis is a crucial tool for understanding the photocatalytic mechanism of prepared materials. The band gap is calculated using Tauc plot[100] (eq 5).

$$\alpha(h\upsilon) = A \times (h\upsilon - E_g)^{n/2} \tag{5}$$

α—absorption coefficient, h—Planck's constant, t—light frequency, A—constant's value, E_g—bandgap energy, and n—number of transitions in the semiconductor. The formula mentioned above is used to compute the bandgap. The bandgap of Co_3O_4, CQD, and Co_3O_4−CQD is computed using the formula mentioned above. The obtained values are 2.68, 3.20, and 2.24 eV, respectively, as shown in Figure 16.

Moreover, the valence band (VB) and conductance band (CB) potential ranges are calculated using the following eqs 6−8[101,102]

$$E_{CB} = \chi - E_c - 0.5E_g \tag{6}$$

$$E_{VB} = E_{CB} + E_g \tag{7}$$

$$\chi = [\chi A^a \chi B^b \chi C^c]^{1/(a+b+c)} \tag{8}$$

where E_{CB} and E_{VB} are edge potentials, E_g is the band gap of the semiconductor material, E_c is the energy of free electrons on the hydrogen scale (4.5 eV), χ represents the Mulliken electronegativity, and a, b, and c represent the number of atoms in the compound. The calculated electronegativity of the Co_3O_4, CQD, and Co_3O_4−CQD is 5.9, 7.5, and 6.7 eV respectively. The E_{CB} and E_{VB} values are calculated with the help of χ and E_g and summarized in Table 2. Figure 17 demonstrates the energy level diagram of the Co_3O_4, CQD, and Co_3O_4−CQD composite.

https://doi.org/10.1021/acsomega.3c09594
ACS Omega 2024, 9, 14101−14117

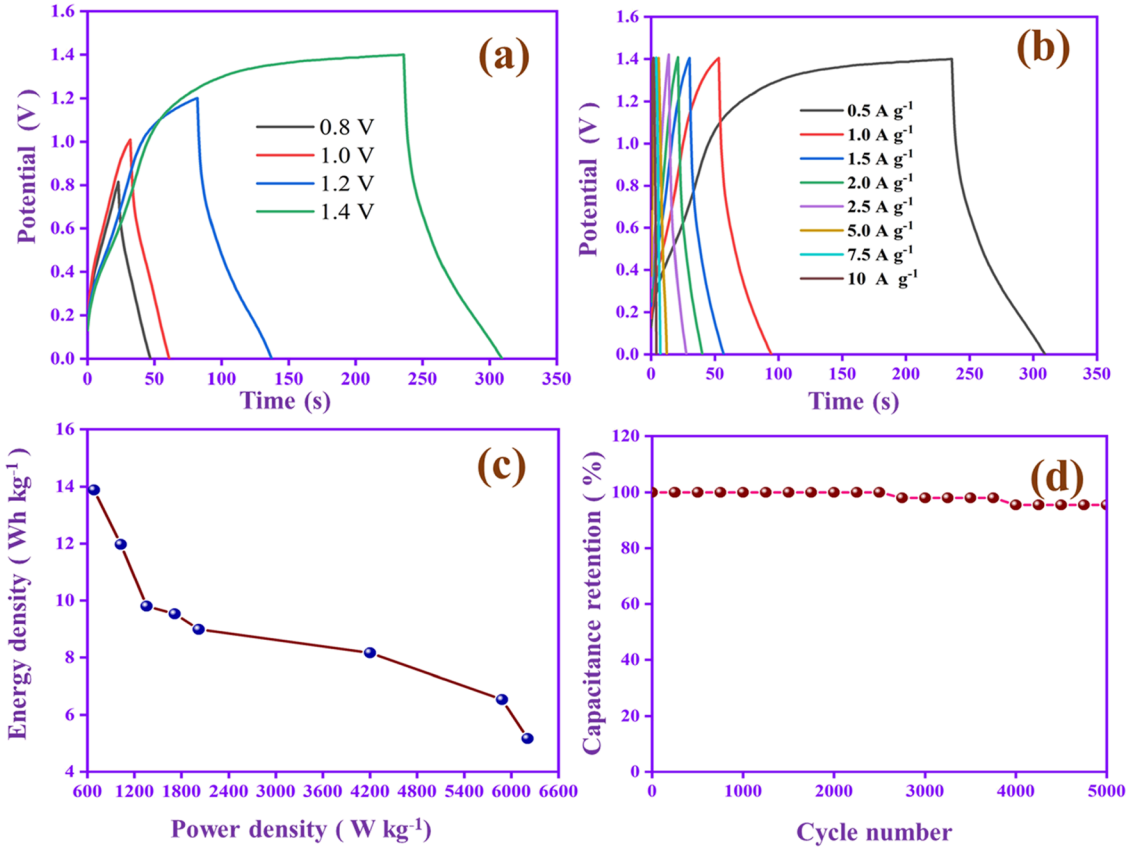

Figure 13. (a) Different voltage GCD, (b) different current density GCD, (c) Ragone diagram, and (d) cycle stability study of Co_3O_4−CQD//AC asymmetric two electrode devices.

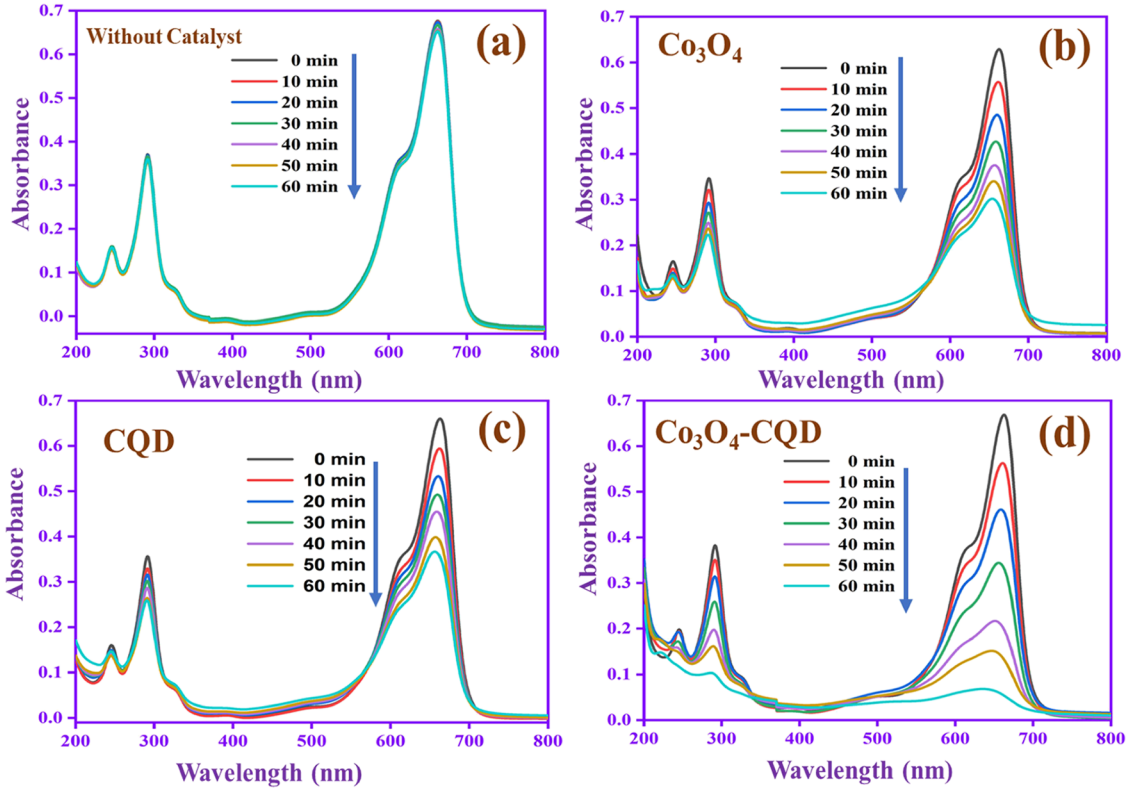

Figure 14. Photocatalytic performance of (a). Without catalyst, (b). Co_3O_4, (c). CQD, (d). Co_3O_4−CQD under UV irradiation for about 60 min.

https://doi.org/10.1021/acsomega.3c09594
ACS Omega 2024, 9, 14101−14117

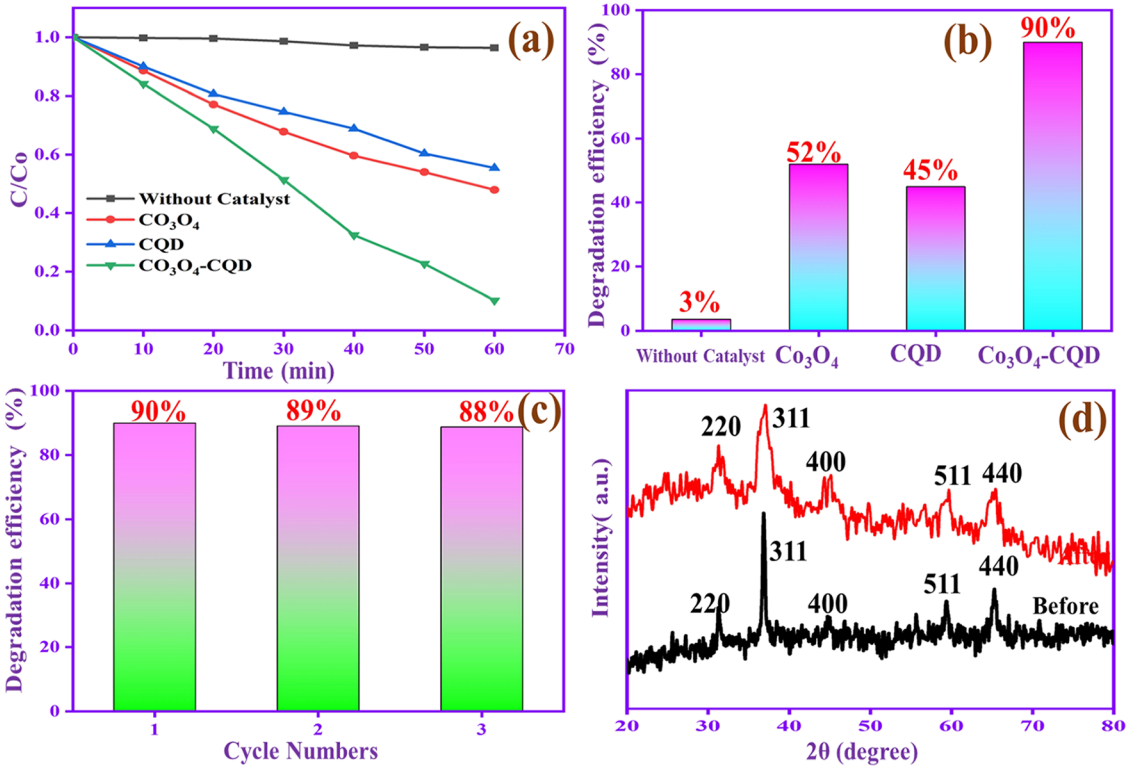

Figure 15. (a) Comparative degradation rate of MB dye under UV irradiation. (b) Degradation efficiency of dye degradation based on different catalysts. (c) Percentage of dye degradation in Co_3O_4−CQD at different cycles of reuse. (d) XRD pattern of Co_3O_4−CQD before and after dye degradation.

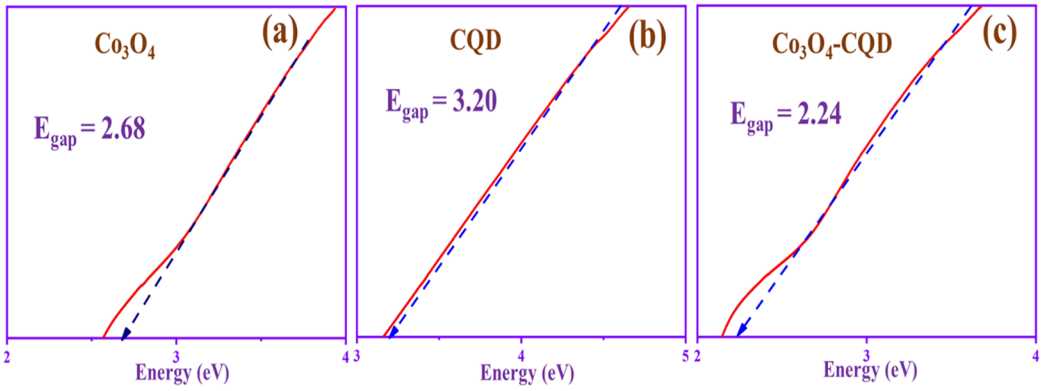

Figure 16. Band gap study of (a) Co_3O_4, (b) CQD, and (c) Co_3O_4−CQD composites.

Table 2. Values of the Bandgap (E_g), Conduction Band (E_{CB}), and Valence Band (E_{VB}) Edge Potentials

materials	E_g (eV)	E_{CB} (V)	E_{VB} (V)
Co_3O_4	2.68	0.06	2.74
CQD	3.20	1.74	4.94
Co_3O_4−CQD	2.24	1.14	3.30

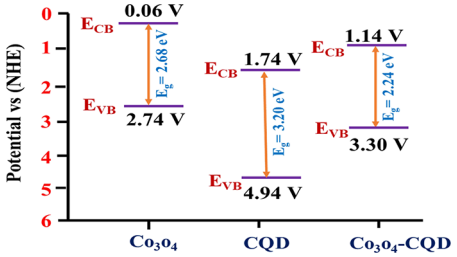

Figure 17. Band gap structure of Co_3O_4, CQD and Co_3O_4−CQD composite.

Figure 18 illustrates the possible mechanism of dye degradation and charge transfer process between Co_3O_4 and CQD. During the photodegradation process under UV light irradiation, the Co_3O_4 and CQD in the Co_3O_4−CQD composite absorb the photon energy. In the first step, Co_3O_4 absorbs the UV light and excites the electron from the VB to the CB, creating an electron (e^-) in the CB and holes (h^+) in the VB. The CB electron of Co_3O_4 can transfer to the CQD CB, while the CQD also undergoes an excitation process and produces electrons and holes in the CB and VB band, respectively. The electrons that are collected during the photocatalytic[103] process are trapped by the oxygen vacancy.

https://doi.org/10.1021/acsomega.3c09594
ACS Omega 2024, 9, 14101−14117

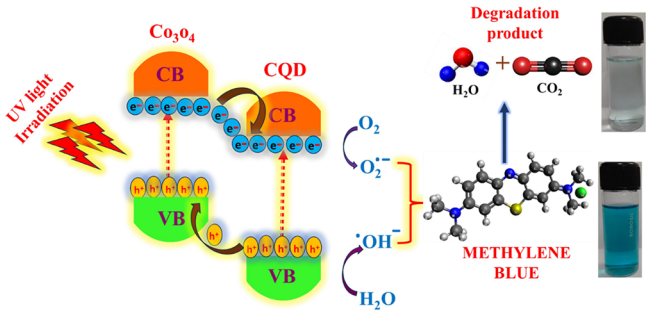

Figure 18. Schematic diagram of dye degradation and the electron charge transfer mechanism of Co_3O_4−CQD under UV irradiation.

This helps to prevent the recombination of electron−hole pairs (e^-/ h^+), which, in turn, enhances the photocatalytic activity. During the reduction process, the electrons react with H_2O to produce the $O_2^{\cdot-}$ and $^{\cdot}OH$ radicals. On the other hand, during the oxidation process, the holes react with H_2O to produce $^{\cdot}OH$ radicals. These radicals play a crucial role in the degradation of MB, breaking down its aromatic bonds and converting it into smaller molecules[104] such as CO_2 and H_2O. The photodegradation process of MB in the presence of Co_3O_4−CQD under UV irradiation can be summarized by the following mechanism[105] steps (eqs 9−13).

$$Co_3O_4/CQD + h\nu \rightarrow Co_3O_4(e^-_{(CB)} + h^+_{(VB)})/CQD(e^-_{(CB)} + h^+_{(VB)}) \quad (9)$$

$$Co_3O_4(e^-_{(CB)}) + CQD(e^-_{(CB)}) \rightarrow (e^-_{(CB)}) + CQD(e^-_{(CB)}) + Co_3O_4 \quad (10)$$

$$O_2 + (e^-_{(CB)}) + CQD(e^-_{(CB)}) \rightarrow O_2^{\cdot-} + CQD \quad (11)$$

$$CQD(h^+_{(VB)}) + H_2O \rightarrow H^+ + {}^{\cdot}OH + CQD \quad (12)$$

$$O_2^{\cdot-} + {}^{\cdot}OH + C_{16}H_{18}CN_3SCl(MB) \rightarrow CO_2 + H_2O + \text{degradedproducts} \quad (13)$$

4. CONCLUSIONS

The Co_3O_4−CQD nanocomposite has been successfully synthesized by using the hydrothermal method. The composite has a uniform nanobrush structure, as confirmed by a surface morphology study. SEM and TEM analysis have also verified that the CQD is attached to the outer surface of the cobalt. By using CV, EIS, and GCD techniques, the composite shows significant improvement over Co_3O_4 in terms of charge mobility, capacitance, cycle stability, and rate capability. The material has a high capacitance of 1209 F g^{-1} at 1 A g^{-1}, and it retains 100% of its capacitance after 3000 cycles. Additionally, the asymmetric supercapacitor device delivers 13.88 W h kg^{-1} energy and 684.65 W kg^{-1} power density with a wide voltage window of 0−1.4 V, using Co_3O_4−CQD//AC. Moreover, the Co_3O_4−CQD exhibits 90% dye degradation efficiency under UV light irradiation, thanks to its higher surface area and suitable band gap. These findings suggest that Co_3O_4−CQD is a promising material for energy storage and environmental applications.

■ ASSOCIATED CONTENT

Supporting Information

The Supporting Information is available free of charge at https://pubs.acs.org/doi/10.1021/acsomega.3c09594.

Physical characterization and electrochemical characterization, asymmetric supercapacitor fabrication, photocatalytic activity test, different excitation fluorescence study of CQD (280−380 nm), photographs of CQD in visible and UV light (254 and 365 nm), zeta potential of CQD, TEM images of CQD, nitrogen adsorption−desorption isotherms for CQD and pore size distributions of CQD, XRD patterns of Co_3O_4−CQD before and after 5000 cycles, and XPS deconvoluted spectra of Co_3O_4−CQD before and after 5000 cycles (PDF)

■ AUTHOR INFORMATION

Corresponding Authors

Na'il Saleh − *Department of Chemistry, College of Science, United Arab Emirates University, Al Ain 15551, United Arab Emirates;* orcid.org/0000-0003-3282-1156; Email: n.saleh@uaeu.ac.ae

Stalin Thambusamy − *Department of Industrial Chemistry, Alagappa University, Karaikudi, Tamil Nadu 630 003, India;* orcid.org/0000-0002-0400-4274; Email: stalin.t@alagappauniversity.ac.in

Authors

Esakkimuthu Shanmugasundaram − *Department of Industrial Chemistry, Alagappa University, Karaikudi, Tamil Nadu 630 003, India;* orcid.org/0009-0004-3165-4362

Kannan Vellaisamy − *Department of Industrial Chemistry, Alagappa University, Karaikudi, Tamil Nadu 630 003, India;* orcid.org/0009-0000-4186-5738

Vigneshkumar Ganesan − *Department of Industrial Chemistry, Alagappa University, Karaikudi, Tamil Nadu 630 003, India;* orcid.org/0000-0001-7757-0472

Vimalasruthi Narayanan − *Department of Industrial Chemistry, Alagappa University, Karaikudi, Tamil Nadu 630 003, India;* orcid.org/0009-0005-6884-9507

Complete contact information is available at: https://pubs.acs.org/10.1021/acsomega.3c09594

Notes

The authors declare no competing financial interest.

■ ACKNOWLEDGMENTS

Na'il Saleh acknowledges the financial support by United Arab Emirates University (Grant # 12S106).

■ REFERENCES

(1) Gong, X.; Liu, G.; Li, Y.; Yu, D. Y. W.; Teoh, W. Y. Functionalized-Graphene Composites: Fabrication and Applications in Sustainable Energy and Environment. *Chem. Mater.* **2016**, *28* (22), 8082−8118.

(2) Niu, X.; Li, Y.; Zhou, Q.; Shu, H.; Wang, J. Arsenene-Based Heterostructures: Highly Efficient Bifunctional Materials for Photovoltaics and Photocatalytics. *ACS Appl. Mater. Interfaces* **2017**, *9* (49), 42856−42861.

(3) Zeng, L.; Li, X.; Fan, S.; Mu, J.; Qin, M.; Wang, X.; Gan, G.; Tadé, M.; Liu, S. Seaweed-Derived Nitrogen-Rich Porous Biomass Carbon as Bifunctional Materials for Effective Electrocatalytic Oxygen Reduction and High-Performance Gaseous Toluene Absorbent. *ACS Sustain. Chem. Eng.* **2019**, *7* (5), 5057−5064.

(4) Ali, M. H.; Al Mamun, M. A.; Haque, M. D.; Rahman, M. F.; Hossain, M. K.; Islam, A. Z. M. T. Performance Enhancement of an MoS_2-Based Heterojunction Solar Cell with an In_2Te_3 Back Surface Field: A Numerical Simulation Approach. *ACS Omega* **2023**, *8* (7), 7017−7029.
(5) Esakkimuthu, S.; Manikandan, G.; Khan, M. I.; Vigneshkumar, G.; Vimalasruthi, N.; Kannan, V.; Rajamohan, R.; Stalin, T. Electrospun and Electropolymerized Carbon Nanofiber−Polyaniline−Cu Material as a Hole Transport Material for Organic Solar Cells. *Carbon Lett.* **2023**, *33*, 2233−2235.
(6) Elia, G. A.; Marquardt, K.; Hoeppner, K.; Fantini, S.; Lin, R.; Knipping, E.; Peters, W.; Drillet, J. F.; Passerini, S.; Hahn, R. An Overview and Future Perspectives of Aluminum Batteries. *Adv. Mater.* **2016**, *28* (35), 7564−7579.
(7) Liu, S.; Kang, L.; Jun, S. C. Challenges and Strategies toward Cathode Materials for Rechargeable Potassium-Ion Batteries. *Adv. Mater.* **2021**, *33* (47), No. 2004689.
(8) Say, M. G.; Brett, C. J.; Edberg, J.; Roth, S. V.; Söderberg, L. D.; Engquist, I.; Berggren, M. Scalable Paper Supercapacitors for Printed Wearable Electronics. *ACS Appl. Mater. Interfaces* **2022**, *14* (50), 55850−55863.
(9) Liu, S.; Kang, L.; Zhang, J.; Jun, S. C.; Yamauchi, Y. Sodium Preintercalation-Induced Oxygen-Deficient Hydrated Potassium Manganese Oxide for High-Energy Flexible Mg-Ion Supercapacitors. *NPG Asia Mater.* **2023**, *15* (1), 9.
(10) El Sharkawy, H. M.; Dhmees, A. S.; Tamman, A. R.; El Sabagh, S. M.; Aboushahba, R. M.; Allam, N. K. N-Doped Carbon Quantum Dots Boost the Electrochemical Supercapacitive Performance and Cyclic Stability of MoS_2. *J. Energy Storage.* **2020**, *27*, No. 101078.
(11) Kate, R. S.; Khalate, S. A.; Deokate, R. J. Overview of Nanostructured Metal Oxides and Pure Nickel Oxide (NiO) Electrodes for Supercapacitors: A Review. *J. Alloys Compd.* **2018**, *734*, 89−111.
(12) Zhang, G.; Xiao, X.; Li, B.; Gu, P.; Xue, H.; Pang, H. Transition Metal Oxides with One-Dimensional/One-Dimensional-Analogue Nanostructures for Advanced Supercapacitors. *J. Mater. Chem. A* **2017**, *5*, 8155−8186.
(13) Wang, K.; Li, Q.; Ren, Z.; Li, C.; Chu, Y.; Wang, Z.; Zhang, M.; Wu, H.; Zhang, Q. 2D Metal−Organic Frameworks (MOFs) for High-Performance BatCap Hybrid Devices. *Small* **2020**, *16* (30), No. 2001987.
(14) Wang, K.; Chen, C.; Li, Y.; Hong, Y.; Wu, H.; Zhang, C.; Zhang, Q. Insight into Electrochemical Performance of Nitrogen-Doped Carbon/NiCo-Alloy Active Nanocomposites. *Small* **2023**, *19* (23), No. e2300054.
(15) Wang, K.; Guo, Y.; Zhang, Q. Metal−Organic Frameworks Constructed from Iron-Series Elements for Supercapacitors. *Small Struct.* **2022**, *3*, No. 2100115.
(16) Fong, K. D.; Wang, T.; Smoukov, S. K. Multidimensional Performance Optimization of Conducting Polymer-Based Supercapacitor Electrodes. *Sustain. Energy Fuels.* **2017**, *1* (9), 1857−1874.
(17) Iqbal, M. F.; Ashiq, M. N.; Zhang, M. Design of Metals Sulfides with Carbon Materials for Supercapacitor Applications: A Review. *Energy Technol.* **2021**, *9* (4), No. 2000987.
(18) Ghosh, S.; Jeong, S. M.; Polaki, S. R. A Review on Metal Nitrides/Oxynitrides as an Emerging Supercapacitor Electrode beyond Oxide. *Korean J. Chem. Eng.* **2018**, *35*, 1389−1408.
(19) Ates, M.; Bayrak, Y.; Yoruk, O.; Caliskan, S. Reduced Graphene Oxide/Titanium Oxide Nanocomposite Synthesis via Microwave-Assisted Method and Supercapacitor Behaviors. *J. Alloys Compd.* **2017**, *728*, 541−551.
(20) Mandal, D.; Routh, P.; Nandi, A. K. A New Facile Synthesis of Tungsten Oxide from Tungsten Disulfide: Structure Dependent Supercapacitor and Negative Differential Resistance Properties. *Small* **2018**, *14* (4), No. 1702881.
(21) Xia, Q. X.; Yun, J. M.; Mane, R. S.; Li, L.; Fu, J.; Lim, J. H.; Kim, K. H. Enhanced Electrochemical Activity of Perforated Graphene in Nickel-Oxide-Based Supercapacitors and Fabrication of Potential Asymmetric Supercapacitors. *Sustain. Energy Fuels* **2017**, *1* (3), 529−539.
(22) Suktha, P.; Phattharasupakun, N.; Sawangphruk, M. Transparent Supercapacitors of 2 Nm Ruthenium Oxide Nanoparticles Decorated on a 3D Nitrogen-Doped Graphene Aerogel. *Sustain. Energy Fuels* **2018**, *2* (8), 1799−1805.
(23) Li, Z.; Mi, Y.; Liu, X.; Liu, S.; Yang, S.; Wang, J. Flexible Graphene/MnO_2 Composite Papers for Supercapacitor Electrodes. *J. Mater. Chem.* **2011**, *21* (38), 14706−14711.
(24) Salunkhe, R. R.; Tang, J.; Kamachi, Y.; Nakato, T.; Kim, J. H.; Yamauchi, Y. Asymmetric Supercapacitors Using 3D Nanoporous Carbon and Cobalt Oxide Electrodes Synthesized from a Single Metal-Organic Framework. *ACS Nano* **2015**, *9* (6), 6288−6296.
(25) Xie, L. J.; Wu, J. F.; Chen, C. M.; Zhang, C. M.; Wan, L.; Wang, J. L.; Kong, Q. Q.; Lv, C. X.; Li, K. X.; Sun, G. H. A Novel Asymmetric Supercapacitor with an Activated Carbon Cathode and a Reduced Graphene Oxide-Cobalt Oxide Nanocomposite Anode. *J. Power Sources* **2013**, *242*, 148−156.
(26) Xu, J. M.; Yan, A. L.; Wang, X. C.; Wang, B. Q.; Cheng, J. P. A Review of Cobalt Monoxide and Its Composites for Supercapacitors. *Ceram. Int.* **2021**, *47* (16), 22229−22239.
(27) Chen, Y.; Hu, L.; Wang, M.; Min, Y.; Zhang, Y. Self-Assembled Co_3O_4 Porous Nanostructures and Their Photocatalytic Activity. *Colloids Surfaces A Physicochem. Eng. Asp.* **2009**, *336* (1−3), 64−68.
(28) Warang, T.; Patel, N.; Santini, A.; Bazzanella, N.; Kale, A.; Miotello, A. Pulsed Laser Deposition of Co_3O_4 Nanoparticles Assembled Coating: Role of Substrate Temperature to Tailor Disordered to Crystalline Phase and Related Photocatalytic Activity in Degradation of Methylene Blue. *Appl. Catal. A Gen.* **2012**, *423*−*424*, 21−27.
(29) Ramesh, S.; Karuppasamy, K.; Kim, H. S.; Kim, H. S.; Kim, J. H. Hierarchical Flowerlike 3D Nanostructure of Co_3O_4@MnO_2/N-Doped Graphene Oxide (NGO) Hybrid Composite for a High-Performance Supercapacitor. *Sci. Rep.* **2018**, *8* (1), No. 16543.
(30) Gonçalves, R.; Paiva, R. S.; Lima, T. M.; Paixão, M. W.; Pereira, E. C. Carbon Nitride/Polypyrrole Composite Supercapacitor: Boosting Performance and Stability. *Electrochim. Acta* **2021**, *368*, No. 137570.
(31) Liu, T.; Liu, J.; Zhang, L.; Cheng, B.; Yu, J. Construction of Nickel Cobalt Sulfide Nanosheet Arrays on Carbon Cloth for Performance-Enhanced Supercapacitor. *J. Mater. Sci. Technol.* **2020**, *47*, 113−121.
(32) Numan, A.; Duraisamy, N.; Saiha Omar, F.; Mahipal, Y. K.; Ramesh, K.; Ramesh, S. Enhanced Electrochemical Performance of Cobalt Oxide Nanocube Intercalated Reduced Graphene Oxide for Supercapacitor Application. *RSC Adv.* **2016**, *6* (41), 34894−34902.
(33) Sarkar, A.; Chakraborty, A. K.; Bera, S.; Krishnamurthy, S. Novel Hydrothermal Synthesis of CoS_2/MWCNT Nanohybrid Electrode for Supercapacitor: A Systematic Investigation on the Influence of MWCNT. *J. Phys. Chem. C* **2018**, *122* (32), 18237−18246.
(34) Rabani, I.; Zafar, R.; Subalakshmi, K.; Kim, H. S.; Bathula, C.; Seo, Y. S. A Facile Mechanochemical Preparation of Co_3O_4@g-C_3N_4 for Application in Supercapacitors and Degradation of Pollutants in Water. *J. Hazard. Mater.* **2021**, *407*, No. 124360.
(35) Syed Zainol Abidin, S. N. J.; Mamat, M. S.; Rasyid, S. A.; Zainal, Z.; Sulaiman, Y. Electropolymerization of Poly(3,4-Ethylenedioxythiophene) onto Polyvinyl Alcohol-Graphene Quantum Dot-Cobalt Oxide Nanofiber Composite for High-Performance Supercapacitor. *Electrochim. Acta* **2018**, *261*, 548−556.
(36) Han, M.; Zhu, S.; Lu, S.; Song, Y.; Feng, T.; Tao, S.; Liu, J.; Yang, B. Recent Progress on the Photocatalysis of Carbon Dots: Classification Mechanism and Applications. *Nano Today.* **2018**, *19*, 201−218.
(37) Cao, L.; Yang, S. T.; Wang, X.; Luo, P. G.; Liu, J. H.; Sahu, S.; Liu, Y.; Sun, Y. P. Competitive Performance of Carbon "Quantum" Dots in Optical Bioimaging. *Theranostics* **2012**, *2* (3), 295−301.

https://doi.org/10.1021/acsomega.3c09594
ACS Omega 2024, 9, 14101−14117

(38) Molaei, M. J. Principles, Mechanisms, and Application of Carbon Quantum Dots in Sensors: A Review. *Anal. Methods.* **2020**, *12*, 1266−1287.
(39) Mistry, B.; Machhi, H. K.; Vithalani, R. S.; Patel, D. S.; Modi, C. K.; Prajapati, M.; Surati, K. R.; Soni, S. S.; Jha, P. K.; Kane, S. R. Harnessing the N-Dopant Ratio in Carbon Quantum Dots for Enhancing the Power Conversion Efficiency of Solar Cells. *Sustain. Energy Fuels* **2019**, *3* (11), 3182−3190.
(40) Sahoo, S.; Satpati, A. K.; Sahoo, P. K.; Naik, P. D. Incorporation of Carbon Quantum Dots for Improvement of Supercapacitor Performance of Nickel Sulfide. *ACS Omega* **2018**, *3* (12), 17936−17946.
(41) Arsalani, N.; Ghadimi, L. S.; Ahadzadeh, I.; Tabrizi, A. G.; Nann, T. Green Synthesized Carbon Quantum Dots/Cobalt Sulfide Nanocomposite as Efficient Electrode Material for Supercapacitors. *Energy Fuels* **2021**, *35* (11), 9635−9645.
(42) Wang, X.; Zhang, X.; Han, W.; Mu, X.; Zhang, Y.; Zhao, X.; Chen, Y.; Yang, Z.; Su, Q.; Xie, E.; Lan, W. Embedded Ag Quantum Dots into Interconnected Co_3O_4 Nanosheets Grown on 3D Graphene Networks for High Stable and Flexible Supercapacitors. *Electrochim. Acta* **2017**, *224*, 260−268.
(43) Ke, J.; Li, X.; Zhao, Q.; Liu, B.; Liu, S.; Wang, S. Upconversion Carbon Quantum Dots as Visible Light Responsive Component for Efficient Enhancement of Photocatalytic Performance. *J. Colloid Interface Sci.* **2017**, *496*, 425−433.
(44) Shanmugasundaram, E.; Ganesan, V.; Narayanan, V.; Perumalsamy, M.; Kuppu, S. V.; Guruviah, P. K.; Stalin, T. Preparation and Characterization of Quantum Dot Doped Polyaniline Photoactive Film for Organic Solar Cell Application. *Chem. Phys. Lett.* **2021**, *771*, No. 138517.
(45) Esakkimuthu, S.; Stalin, T. Investigations of the Optical and Electrical Properties of Carbon Quantum Dots Doped Conducting Polymers for Organic Solar Cell Applications. *Indian J. Chem. Technol.* **2022**, *29* (6), 771−775.
(46) Abdallah, A. M.; Awad, R. Study of the Structural and Physical Properties of Co_3O_4 Nanoparticles Synthesized by Co-Precipitation Method. *J. Supercond. Nov. Magn.* **2020**, *33* (5), 1395−1404.
(47) Bankole, O. M.; Olaseni, S. E.; Adeyemo, M. A.; Ogunlaja, A. S. Microwave-Assisted Synthesis of Cobalt Oxide/Reduced Graphene Oxide (Co_3O_4-RGO) Composite and Its Sulfite Enhanced Photocatalytic Degradation of Organic Dyes. *Z. Phys. Chem.* **2020**, *234* (10), 1524.
(48) Gajendiran, J.; Sivakumar, N.; Parthasaradhi Reddy, C.; Ramya, J. R. The Effect of Calcination's Temperature on the Structural, Morphological, Optical Behaviour, Hemocompatibility and Antibacterial Activity of Nanocrystalline Co_3O_4 Powders. *Ceram. Int.* **2020**, *46* (4), 5469−5476.
(49) Vennela, A. B.; Mangalaraj, D.; Muthukumarasamy, N.; Agilan, S.; Hemalatha, K. V. Structural and Optical Properties of Co_3O_4 Nanoparticles Prepared by Sol-Gel Technique for Photocatalytic Application. *Int. J. Electrochem. Sci.* **2019**, *14* (4), 3535−3552.
(50) Packiaraj, R.; Devendran, P.; Venkatesh, K. S.; Asath Bahadur, S.; Manikandan, A.; Nallamuthu, N. Electrochemical Investigations of Magnetic Co_3O_4 Nanoparticles as an Active Electrode for Supercapacitor Applications. *J. Supercond. Nov. Magn.* **2019**, *32* (8), 2427−2436.
(51) Alem, A. F.; Worku, A. K.; Ayele, D. W.; Wubieneh, T. A.; Teshager, A. A.; Kndie, T. M.; Admasu, B. T.; Teshager, M. A.; Asege, A. A.; Ambaw, M. D.; Zeleke, M. A.; Shibesh, A. K.; Yemata, T. A. Ag Doped Co_3O_4 Nanoparticles for High-Performance Supercapacitor Application. *Heliyon* **2023**, *9* (2), No. e13286.
(52) Ren, H.; Ge, L.; Guo, Q.; Li, L.; Hu, G.; Li, J. The Enhancement of Photocatalytic Performance of $SrTiO_3$ Nanoparticles: Via Combining with Carbon Quantum Dots. *RSC Adv.* **2018**, *8* (36), 20157−20165.
(53) Mussa, Y.; Ahmed, F.; Abuhimd, H.; Arsalan, M.; Alsharaeh, E. Enhanced Electrochemical Performance at High Temperature of Cobalt Oxide/Reduced Graphene Oxide Nanocomposites and Its Application in Lithium-Ion Batteries. *Sci. Rep.* **2019**, *9* (1), 44.
(54) Naushad, M.; Ahamad, T.; Ubaidullah, M.; Ahmed, J.; Ghafar, A. A.; Al-Sheetan, K. M.; Arunachalam, P. Nitrogen-Doped Carbon Quantum Dots (N-CQDs)/Co_3O_4 Nanocomposite for High Performance Supercapacitor. *J. King Saud Univ. - Sci.* **2021**, *33* (1), No. 101252.
(55) Chaudhary, S.; Kumar, S.; Kaur, B.; Mehta, S. K. Potential Prospects for Carbon Dots as a Fluorescence Sensing Probe for Metal Ions. *RSC Adv.* **2016**, *6* (93), 90526−90536.
(56) Zhao, Y.; Chen, S.; Sun, B.; Su, D.; Huang, X.; Liu, H.; Yan, Y.; Sun, K.; Wang, G. Graphene-Co_3O_4 Nanocomposite as Electrocatalyst with High Performance for Oxygen Evolution Reaction. *Sci. Rep.* **2015**, *5*, 7629.
(57) Zheng, C.; Huang, L.; Guo, Q.; Chen, W.; Li, W.; Wang, H. Facile One-Step Fabrication of Upconversion Fluorescence Carbon Quantum Dots Anchored on Graphene with Enhanced Nonlinear Optical Responses. *RSC Adv.* **2018**, *8* (19), 10267−10276.
(58) Patil, U. M.; Ghorpade, R. V.; Nam, M. S.; Nalawade, A. C.; Lee, S.; Han, H.; Jun, S. C. PolyHIPE Derived Freestanding 3D Carbon Foam for Cobalt Hydroxide Nanorods Based High Performance Supercapacitor. *Sci. Rep.* **2016**, *6*, No. 35490.
(59) Omer, K. M.; Tofiq, D. I.; Hassan, A. Q. Solvothermal Synthesis of Phosphorus and Nitrogen Doped Carbon Quantum Dots as a Fluorescent Probe for Iron(III). *Microchim. Acta* **2018**, *185* (10), 466.
(60) Liu, Y.; Chang, X.; Wang, M.; Guo, H.; Li, W.; Wang, Y. Hierarchical $CuCo_2O_4$/CuO Nanoflowers Crosslinked with Carbon Nanotubes as an Advanced Electrode for Supercapacitors. *J. Alloys Compd.* **2021**, *871*, No. 159555.
(61) Liu, S.; Yin, Y.; Shen, Y.; Hui, K. S.; Chun, Y. T.; Kim, J. M.; Hui, K. N.; Zhang, L.; Jun, S. C. Phosphorus Regulated Cobalt Oxide@Nitrogen-Doped Carbon Nanowires for Flexible Quasi-Solid-State Supercapacitors. *Small* **2020**, *16* (4), No. 1906458.
(62) Kang, L.; Huang, C.; Zhang, J.; Zhang, M.; Zhang, N.; Liu, S.; Ye, Y.; Luo, C.; Gong, Z.; Wang, C.; Zhou, X.; Wu, X.; Jun, S. C. Effect of Fluorine Doping and Sulfur Vacancies of $CuCo_2S_4$ on Its Electrochemical Performance in Supercapacitors. *Chem. Eng. J.* **2020**, *390*, No. 124643.
(63) Zheng, H.; Niu, P.; Zhao, Z. Carbon Quantum Dot Sensitized Pt@Bi_2WO_6/FTO Electrodes for Enhanced Photoelectro-Catalytic Activity of Methanol Oxidation. *RSC Adv.* **2017**, *7* (43), 26943−26951.
(64) Liu, Y. B.; Lin, L. Y.; Huang, Y. Y.; Tu, C. C. Investigation of the Electroactive Capability for the Supercapacitor Electrode with Cobalt Oxide Rhombus Nanopillar and Nanobrush Arrays. *J. Power Sources* **2016**, *315*, 23−34.
(65) Kang, X.; Wu, L.; Xu, J.; Liu, D.; Song, Q.; Hu, Y. Preparation and Photoelectrochemical Properties of Porous Silicon/Carbon Dots Composites. *IOP Conf. Ser.: Mater. Sci. Eng.* **2020**, *892*, No. 012025, DOI: 10.1088/1757-899X/892/1/012025.
(66) Yang, W.; Gao, Z.; Ma, J.; Wang, J.; Wang, B.; Liu, L. Effects of Solvent on the Morphology of Nanostructured Co_3O_4 and Its Application for High-Performance Supercapacitors. *Electrochim. Acta* **2013**, *112*, 378−385.
(67) Chakraborty, P.; Deka, N.; Patra, D. C.; Debnath, K.; Mondal, S. P. Hydrothermally Grown Porous Cobalt Oxide Nanostructures for Enzyme-Less Glucose Detection. *J. Electron. Mater.* **2021**, *50* (6), 3699−3705.
(68) Raeisi, M.; Alijani, H. Q.; Peydayesh, M.; Khatami, M.; Bagheri Baravati, F.; Borhani, F.; Slouf, M.; Soltaninezhad, S. Magnetic Cobalt Oxide Nanosheets: Green Synthesis and in Vitro Cytotoxicity. *Bioprocess Biosyst. Eng.* **2021**, *44* (7), 1423−1432.
(69) Fan, H.; Yi, G.; Tian, Q.; Zhang, X.; Xing, B.; Zhang, C.; Chen, L.; Zhang, Y. Hydrothermal-Template Synthesis and Electrochemical Properties of Co_3O_4/Nitrogen-Doped Hemisphere-Porous Graphene Composites with 3D Heterogeneous Structure. *RSC Adv.* **2020**, *10* (60), 36794−36805.
(70) Xie, S.; Liu, Y.; Deng, J.; Yang, J.; Zhao, X.; Han, Z.; Zhang, K.; Dai, H. Insights into the Active Sites of Ordered Mesoporous Cobalt

Oxide Catalysts for the Total Oxidation of O-Xylene. *J. Catal.* **2017**, *352*, 282−292.
(71) Wang, Y.; Zhong, Z.; Chen, Y.; Ng, C. T.; Lin, J. Controllable Synthesis of Co_3O_4 from Nanosize to Microsize with Large-Scale Exposure of Active Crystal Planes and Their Excellent Rate Capability in Supercapacitors Based on the Crystal Plane Effect. *Nano Res.* **2011**, *4* (7), 695−704.
(72) Rakhi, R. B.; Chen, W.; Cha, D.; Alshareef, H. N. Substrate Dependent Self-Organization of Mesoporous Cobalt Oxide Nanowires with Remarkable Pseudocapacitance. *Nano Lett.* **2012**, *12* (5), 2559−2567.
(73) Xu, J.; Xu, C.; Zhao, Y.; Wu, J.; Hu, J. Hollow Co_3O_4@MnO_2 Cubic Derived From ZIF-67@Mn-ZIF as Electrode Materials for Supercapacitors. *Front. Chem.* **2019**, *7*, 831.
(74) Yang, J.; Xu, X.; Zhou, X.; Jiang, S.; Chen, W.; Shi, S.; Wang, D.; Liu, Z. Ultrasmall Co_3O_4 Nanoparticles Confined in P, N-Doped Carbon Matrices for High-Performance Supercapacitors. *J. Phys. Chem. C* **2020**, *124* (17), 9225−9232.
(75) Zallouz, S.; Réty, B.; Vidal, L.; Le Meins, J. M.; Matei Ghimbeu, C. Co_3O_4 Nanoparticles Embedded in Mesoporous Carbon for Supercapacitor Applications. *ACS Appl. Nano Mater.* **2021**, *4* (5), 5022−5037.
(76) Ding, Y.; Peng, Y.; Chen, S.; Li, Z.; Zhang, X.; Falaras, P.; Hu, L. A Competitive Coordination Strategy to Synthesize Co_3O_4@carbon Flower-like Structures for High-Performance Asymmetric Supercapacitors. *Appl. Surf. Sci.* **2019**, *495*, No. 143502.
(77) Wu, C. L.; Chen, D. H. Fabrication of RGO/CoSx-RGO/RGO Hybrid Film via Coassembly and Sulfidation of 2D Metal Organic Framework Nanoflakes and Graphene Oxide as Free-Standing Supercapacitor Electrode. *J. Alloys Compd.* **2021**, *872*, No. 159702.
(78) Liu, S.; Ni, D.; Li, H. F.; Hui, K. N.; Ouyang, C. Y.; Jun, S. C. Effect of Cation Substitution on the Pseudocapacitive Performance of Spinel Cobaltite MCo_2O_4 (M = Mn, Ni, Cu, and Co). *J. Mater. Chem. A* **2018**, *6* (23), 10674−10685.
(79) Wang, X.; Wang, Y.; Jiang, Y.; Li, X.; Liu, Y.; Xiao, H.; Ma, Y.; Huang, Y.; Yuan, G. Tailoring Ultrahigh Energy Density and Stable Dendrite-Free Flexible Anode with $Ti_3C_2T_x$ MXene Nanosheets and Hydrated Ammonium Vanadate Nanobelts for Aqueous Rocking-Chair Zinc Ion Batteries. *Adv. Funct. Mater.* **2021**, *31* (35), No. 2103210.
(80) Liu, S.; Kang, L.; Hu, J.; Jung, E.; Henzie, J.; Alowasheeir, A.; Zhang, J.; Miao, L.; Yamauchi, Y.; Jun, S. C. Realizing Superior Redox Kinetics of Hollow Bimetallic Sulfide Nanoarchitectures by Defect-Induced Manipulation toward Flexible Solid-State Supercapacitors. *Small* **2022**, *18* (5), No. 2104507.
(81) Liu, S.; Yin, Y.; Ni, D.; Hui, K. S.; Ma, M.; Park, S.; Hui, K. N.; Ouyang, C. Y.; Jun, S. C. New Insight into the Effect of Fluorine Doping and Oxygen Vacancies on Electrochemical Performance of Co_2MnO_4 for Flexible Quasi-Solid-State Asymmetric Supercapacitors. *Energy Storage Mater.* **2019**, *22*, 384−396.
(82) Zhang, Y. S.; Lu, C.; Hu, Y. X.; Zhang, B. M.; Li, J.; Tian, C. Y.; Zhang, D. T.; Kong, L. B.; Liu, M. C. Assemble from 0D to 3D: Anchored 0D Molybdenum Carbide on 3D Octahedral Amorphous Carbon with Excellent Capacitive Properties. *J. Mater. Sci.* **2020**, *55* (32), 15562−15573.
(83) Liu, S.; Yin, Y.; Hui, K. S.; Hui, K. N.; Lee, S. C.; Jun, S. C. High-Performance Flexible Quasi-Solid-State Supercapacitors Realized by Molybdenum Dioxide@Nitrogen-Doped Carbon and Copper Cobalt Sulfide Tubular Nanostructures. *Adv. Sci.* **2018**, *5* (10), No. 1800733.
(84) Xie, Y. Synthesis and Electrochemical Performance of an Electroactive Nitrogen-Doping SnO_2 Nanoarray Supported on Carbon Fiber. *J. Chem. Res.* **2021**, *45* (7−8), 738−746, DOI: 10.1177/1747519821994252.
(85) Liu, S.; Lee, S. C.; Patil, U.; Shackery, I.; Kang, S.; Zhang, K.; Park, J. H.; Chung, K. Y.; Chan Jun, S. Hierarchical MnCo-Layered Double Hydroxides@Ni$(OH)_2$ Core-Shell Heterostructures as Advanced Electrodes for Supercapacitors. *J. Mater. Chem. A* **2017**, *5* (3), 1043−1049.
(86) Mugheri, A. Q.; Tahira, A.; Aftab, U.; Abro, M. I.; Mallah, A. B.; Memon, G. Z.; Khan, H.; Abbasi, M. A.; Halepoto, I. A.; Chaudhry, S. R.; Ibupoto, Z. H. An Advanced and Efficient Co_3O_4/C Nanocomposite for the Oxygen Evolution Reaction in Alkaline Media. *RSC Adv.* **2019**, *9* (59), 34136−34143.
(87) Li, J.; Cui, M.; Lai, Y.; Zhang, Z.; Lu, H.; Fang, J.; Liu, Y. Investigation of Polyaniline Co-Doped with Zn^{2+} and H^+ as the Electrode Material for Electrochemical Supercapacitors. *Synth. Met.* **2010**, *160* (11−12), 1228−1233.
(88) Zhang, M.; Liu, W.; Liang, R.; Tjandra, R.; Yu, A. Graphene Quantum Dot Induced Tunable Growth of Nanostructured $MnCo_2O_4$ Composites for High-Performance Supercapacitors. *Sustain. Energy Fuels* **2019**, *3* (9), 2499−2508.
(89) Lv, H.; Yuan, Y.; Xu, Q.; Liu, H.; Wang, Y. G.; Xia, Y. Carbon Quantum Dots Anchoring MnO_2/Graphene Aerogel Exhibits Excellent Performance as Electrode Materials for Supercapacitor. *J. Power Sources* **2018**, *398*, 167−174.
(90) Ghosh, K.; Srivastava, S. K. Enhanced Supercapacitor Performance and Electromagnetic Interference Shielding Effectiveness of CuS Quantum Dots Grown on Reduced Graphene Oxide Sheets. *ACS Omega* **2021**, *6* (7), 4582−4596.
(91) De, B.; Kuila, T.; Kim, N. H.; Lee, J. H. Carbon Dot Stabilized Copper Sulphide Nanoparticles Decorated Graphene Oxide Hydrogel for High Performance Asymmetric Supercapacitor. *Carbon N. Y.* **2017**, *122*, 247−257.
(92) Prasath, A.; Athika, M.; Duraisamy, E.; Sharma, A. S.; Elumalai, P. Carbon-Quantum-Dot-Derived Nanostructured MnO_2 and Its Symmetrical Supercapacitor Performances. *ChemistrySelect.* **2018**, *3* (30), 8713−8723.
(93) Prasath, A.; Athika, M.; Duraisamy, E.; Selva Sharma, A.; Sankar Devi, V.; Elumalai, P. Carbon Quantum Dot-Anchored Bismuth Oxide Composites as Potential Electrode for Lithium-Ion Battery and Supercapacitor Applications. *ACS Omega* **2019**, *4* (3), 4943−4954.
(94) Lv, H.; Gao, X.; Xu, Q.; Liu, H.; Wang, Y. G.; Xia, Y. Carbon Quantum Dot-Induced MnO_2 Nanowire Formation and Construction of a Binder-Free Flexible Membrane with Excellent Superhydrophilicity and Enhanced Supercapacitor Performance. *ACS Appl. Mater. Interfaces.* **2017**, *9* (46), 40394−40403.
(95) Zhu, Y.; Ji, X.; Pan, C.; Sun, Q.; Song, W.; Fang, L.; Chen, Q.; Banks, C. E. A Carbon Quantum Dot Decorated RuO_2 Network: Outstanding Supercapacitances under Ultrafast Charge and Discharge. *Energy Environ. Sci.* **2013**, *6* (12), 3665−3675.
(96) Ashourdan, M.; Semnani, A.; Hasanpour, F.; Moosavifard, S. E. Synthesis of $CuMnO_2$/Graphene Quantum Dot Nanocomposites as Novel Electrode Materials for High Performance Supercapacitors. *J. Energy Storage* **2021**, *36*, No. 102449.
(97) Zhang, C.; Xiao, J.; Lv, X.; Qian, L.; Yuan, S.; Wang, S.; Lei, P. Hierarchically Porous Co_3O_4/C Nanowire Arrays Derived from a Metal-Organic Framework for High Performance Supercapacitors and the Oxygen Evolution Reaction. *J. Mater. Chem. A* **2016**, *4* (42), 16516−16523.
(98) Khan, M. A. M.; Khan, W.; Ahamed, M.; Ahmed, J.; Al-Gawati, M. A.; Alhazaa, A. N. Silver-Decorated Cobalt Ferrite Nanoparticles Anchored onto the Graphene Sheets as Electrode Materials for Electrochemical and Photocatalytic Applications. *ACS Omega* **2020**, *5* (48), 31076−31084.
(99) Wang, Q.; Li, J.; Tu, X.; Liu, H.; Shu, M.; Si, R.; Ferguson, C. T. J.; Zhang, K. A. I.; Li, R. Single Atomically Anchored Cobalt on Carbon Quantum Dots as Efficient Photocatalysts for Visible Light-Promoted Oxidation Reactions. *Chem. Mater.* **2020**, *32* (2), 734−743.
(100) Shanmugasundaram, E.; Ganesan, V.; Narayanan, V.; Vellaisamy, K.; Rajamohan, R.; Lee, Y. R.; Kaliyamoorthy, S.; Thambusamy, S. Heteroatom (Boron, Nitrogen, and Fluorine) Quantum Dot-Doped Polyaniline-Photoactive Film Preparation and Characterization for Organic Solar Cell Applications. *New J. Chem.* **2023**, *47*, 13127−13137.
(101) Peng, P.; Chen, Z.; Li, X.; Wu, Y.; Xia, Y.; Duan, A.; Wang, D.; Yang, Q. Biomass-Derived Carbon Quantum Dots Modified

Bi_2MoO_6/Bi_2S_3 Heterojunction for Efficient Photocatalytic Removal of Organic Pollutants and Cr (VI). *Sep. Purif. Technol.* **2022**, *291*, No. 120901.
(102) Yan, M.; Wu, Y.; Zhu, F.; Hua, Y.; Shi, W. The Fabrication of a Novel Ag_3VO_4/WO_3 Heterojunction with Enhanced Visible Light Efficiency in the Photocatalytic Degradation of TC. *Phys. Chem. Chem. Phys.* **2016**, *18* (4), 3308−3315.
(103) Asaithambi, S.; Sakthivel, P.; Karuppaiah, M.; Yuvakkumar, R.; Velauthapillai, D.; Ahamad, T.; Khan, M. A. M.; Mohammed, M. K. A.; Vijayaprabhu, N.; Ravi, G. The Bifunctional Performance Analysis of Synthesized Ce Doped SnO_2/g-C_3N_4 Composites for Asymmetric Supercapacitor and Visible Light Photocatalytic Applications. *J. Alloys Compd.* **2021**, *866*, No. 158807.
(104) Ayu, D. G.; Gea, S.; Andriayani, N.; Telaumbanua, D. J.; Piliang, A. F. R.; Harahap, M.; Yen, Z.; Goei, R.; Tok, A. I. Y. Photocatalytic Degradation of Methylene Blue Using N-Doped ZnO/Carbon Dot (N-ZnO/CD) Nanocomposites Derived from Organic Soybean. *ACS Omega* **2023**, *8* (17), 14965−14984.
(105) Asaithambi, S.; Sakthivel, P.; Karuppaiah, M.; Balamurugan, K.; Yuvakkumar, R.; Thambidurai, M.; Ravi, G. Synthesis and Characterization of Various Transition Metals Doped SnO_2@MoS_2 Composites for Supercapacitor and Photocatalytic Applications. *J. Alloys Compd.* **2021**, *853*, No. 157060.

https://doi.org/10.1021/acsomega.3c09594
ACS Omega 2024, 9, 14101−14117